Bio-Design and Manufacturing (2024) 7:701–720
https://doi.org/10.1007/s42242-024-00304-3

RESEARCH ARTICLE

Enhanced axonal regeneration and functional recovery of the injured sciatic nerve in a rat model by lithium-loaded electrospun nanofibrous scaffolds

Banafsheh Dolatyar[1] · **Bahman Zeynali**[1] · **Iman Shabani**[2] · **Azita Parvaneh Tafreshi**[1,3] · **Reza Karimi-Soflou**[2]

Received: 6 October 2023 / Accepted: 14 June 2024

Abstract

Increasing evidence indicates that engineered nerve grafts have great potential for the regeneration of peripheral nerve injuries (PNIs). While most studies have focused only on the topographical features of the grafts, we have considered both the biophysical and biochemical manipulations in our applied nanoscaffold. To achieve this, we fabricated an electrospun nanofibrous scaffold (ENS) containing polylactide nanofibers loaded with lithium (Li) ions, a Wnt/β-catenin signaling activator. In addition, we seeded human adipose-derived mesenchymal stem cells (hADMSCs) onto this engineered scaffold to examine if their differentiation toward Schwann-like cells was induced. We further examined the efficacy of the scaffolds for nerve regeneration in vivo via grafting in a PNI rat model. Our results showed that Li-loaded ENSs gradually released Li within 11 d, at concentrations ranging from 0.02 to (3.64 ± 0.10) mmol/L, and upregulated the expression of Wnt/β-catenin target genes (*cyclinD1* and *c-Myc*) as well as those of Schwann cell markers (growth-associated protein 43 (GAP43), S100 calcium binding protein B (S100B), glial fibrillary acidic protein (GFAP), and SRY-box transcription factor 10 (SOX10)) in differentiated hADMSCs. In the PNI rat model, implantation of Li-loaded ENSs with/without cells improved behavioral features such as sensory and motor functions as well as the electrophysiological characteristics of the injured nerve. This improved function was further validated by histological analysis of sciatic nerves grafted with Li-loaded ENSs, which showed no fibrous connective tissue but enhanced organized myelinated axons. The potential of Li-loaded ENSs in promoting Schwann cell differentiation of hADMSCs and axonal regeneration of injured sciatic nerves suggests their potential for application in peripheral nerve tissue engineering.

Graphic abstract

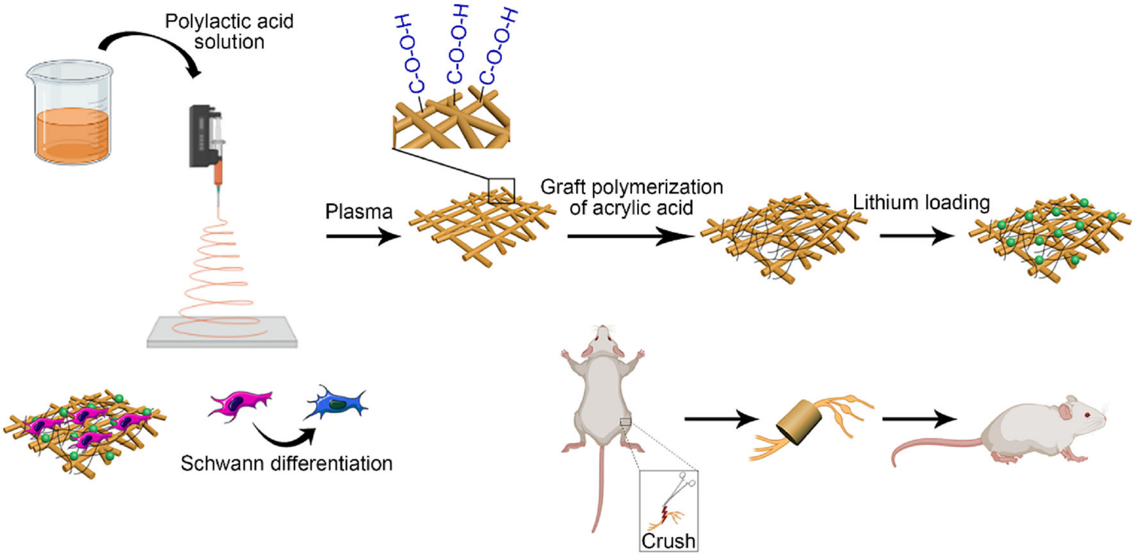

Keywords Stem cell · Schwann cell differentiation · Electrospun nanofibrous scaffold · Lithium ion · Nerve regeneration

Introduction

Peripheral nerve injury (PNI) is one of the greatest health concerns in patients with multiple traumas [1]. Despite the claimed self-repair ability of the peripheral nerves, the average axonal regeneration rate is too slow (1 mm/d) in patients with lifelong disability [2]. The available therapeutic strategies, such as autografting as the gold standard treatment, present many obstacles and often have unsatisfactory outcomes [2]. Therefore, PNI repair remains the foremost challenge in clinical and translational neurosciences, and an accurate and authentic alternative approach is urgently required. Cell-based therapies have provided satisfactory regenerative results with low invasiveness [3]. Because of the pivotal role of Schwann cells in the regeneration processes of injured peripheral nerves, including axonal regrowth and remyelination [4], their engraftment in PNI is plausible. Nevertheless, autografting (either autologous Schwann cells or nerve grafts) is not only invasive but also requires the availability of a healthy nerve [5]. To overcome these obstacles, several artificial and biological nerve grafts have been introduced in the past few decades due to the great progress in tissue engineering [6]. Increasing evidence has demonstrated that engineered nerve grafts are suitable and attractive alternatives to natural autografts [7]. However, most of the previous reports have focused on the topographical features of the grafts [8] rather than on the improvement of the biophysical and biochemical potentials of the grafts through proper design and fabrication of the scaffolds.

Owing to the important function of the Wnt/β-catenin signaling pathway in neural development, as well as its role in Schwann cell-specific gene expression [9], myelin-specific gene expression [10], and axonal sorting in Schwann cell development [11], we sought to use lithium (Li) as a general Wnt/β-catenin activator in our study. Li salt has a 50-year pharmaceutical history as an antidepressant and mood stabilizer for treating mental disorders such as bipolar disorder [12, 13]. Increasing evidence suggests that Li has anti-inflammatory [14], antiapoptotic [15], and neuroprotective [16, 17] effects and induces axon regeneration [18]. It has been considered as a treatment for neurodegenerative diseases, including Alzheimer's [19], Parkinson's [20], and Huntington's [21] diseases, amyotrophic lateral sclerosis [22], and multiple sclerosis [23]. The improving effects of Li ions on myelinogenesis and PNI recovery have been well documented [6, 10, 24, 25]. Its administration has been performed either as an additive to the cell culture medium [26], systemic injection in vivo (intraperitoneal [27] or intravenous [28]), or orally in drinking water [24]. Local injection of Li just after the induced injury for peripheral nerve regeneration in a rodent sciatic nerve injury model was reported by Lin et al. [29]. Despite the reduced off-target effects and enhanced therapeutic efficacy through local Li delivery into the injury site, toxicity may occur due to the accumulation of large amounts of Li within a short time. Therefore, in this study, we aimed to design a Li-loaded nanofibrous scaffold with sustained Li release that would generate a proper scaffold for PNI regeneration applications. The sustained availability of Li should activate the Wnt/β-catenin signaling pathway and enhance Schwann cell-like cell (SCLC) differentiation and myelin gene expression, which could be applied in vivo in a rat model of sciatic nerve injury.

Using the ion-exchange method [30], we fabricated a Li-loaded polylactide (PLA) nanofibrous scaffold and investigated the effects of this bioactive scaffold on SCLC differentiation in human adipose-derived mesenchymal stem cells (hADMSCs) in vitro and on axon regeneration in an animal model of PNI in vivo.

Materials and methods

Cell isolation, culture, and differentiation

Primary human MSCs were isolated using liposuctioned abdominal fat obtained from consenting female patients (age range: 30–35 years old). hADMSCs were isolated using 0.1% (1 g/L) collagenase type I (Gibco, USA) as described previously [31], after which they were expanded by serial passages in Dulbecco's modified Eagle's medium (DMEM) supplemented with 10% (volume fraction) fetal bovine serum (FBS), 1% (volume fraction) GlutaMAX™-I, and 1% (0.01 g/mL) penicillin/streptomycin. hADMSCs Passages 3–5 were conducted. To differentiate hADMSCs into SCLCs, our previously described protocol was carried out [32].

Characterization of hADMSCs

Flow cytometry

The Passage 3 (P3) hADMSCs were washed in phosphate-buffered saline (PBS), fixed with 4% (0.04 g/mL) paraformaldehyde, blocked with 3% (0.03 g/mL) bovine serum albumin (BSA), and incubated at 4 °C for 30 min with antibodies against cluster of differentiation 73 (CD73) (fluorescein isothiocyanate (FITC); BD Biosciences), CD45 (FITC; eBioscience), CD105 (PerCP-Immunostep), and CD90 (FITC; Exbio). They were then washed three times in cold PBS and analyzed using an FACS Calibur flow cytometer (BD Biosciences).

Extended author information available on the last page of the article

Differentiation of osteogenic, adipogenic, and chondrogenic lineages

To induce differentiation, hADMSCs were first cultured until they reached 70%–80% confluence; then, the normal medium was removed, and differentiation medium was added. For osteogenic differentiation, hADMSCs were cultured for 21 d in osteogenic differentiation medium (high-glucose DMEM (DMEM-HG) including 10% FBS, 50 mg/mL ascorbic acid 2-phosphate, 10 nmol/L dexamethasone, and 10 mmol/L beta-glycerol phosphate), stained with alizarin red as described previously [33], and visualized under a phase contrast microscope (B510 Optika, Italy). To induce adipogenic differentiation, hADMSCs were cultured for 21 d in adipogenic differentiation medium (DMEM-HG including 10% FBS, 50 mg/mL indomethacin, and 100 nmol/L dexamethasone), stained with oil red O as described previously [34], and visualized under a phase contrast microscope. For chondrogenic differentiation, hADMSCs were cultured for 21 d in chondrogenic differentiation medium (DMEM-HG including 10% FBS, 10 ng/mL TGF-beta, 0.1 mmol/L dexamethasone, 100 μg/mL sodium pyruvate, 50 mg/mL ascorbic acid 2-phosphate, and 50 mg/mL insulin-transferrin-selenium), stained with toluidine blue O (TBO) as described previously [35], and observed under a phase contrast microscope.

Differentiation of hADMSCs into SCLCs

To induce hADMSCs into the Schwann cell (SC) lineage, cells were first cultured in preinduction medium (DMEM/F12 supplemented with basic fibroblast growth factor (bFGF), epidermal growth factor (EGF), and B27) for 7 d to produce spheroids, after which the spheroids were singled and exposed to complete induction medium (DMEM/F12 supplemented with FBS, forskolin, platelet-derived growth factor (PDGF), heregulin, and bFGF) for a further 7 d.

Immunofluorescence staining

To investigate the differentiation potential of hADMSCs, the expression of Schwann cell-specific markers (SOX10, GFAP, and GAP43) was examined using immunofluorescence staining as described previously [36]. The primary antibodies were anti-SOX10 (1:500, volume ratio), anti-GFAP (1:300, volume ratio), and anti-GAP43 (1:500, volume ratio) (all from Abcam, UK). Goat antimouse FITC (1:500, volume ratio; Abcam, UK) and secondary antibody were used. Cells were visualized and imaged using an inverted fluorescence microscope (Zeiss inverted fluorescence microscope, Germany).

RNA isolation and quantitative real-time polymerase chain reaction (PCR)

Total RNA was extracted using TRIzol reagent (Invitrogen, Paisley, UK) and converted to complementary DNA (cDNA) using a reverse transcriptase enzyme (Yekta Tajhiz Azma, Iran) according to the manufacturer's protocol. Real-time PCR and quantification of gene expression were performed as explained previously [36]. The primer sequences are shown in Table S1 (Supplementary Information).

Scaffold fabrication and characterization

Polylactide (PLA) nanofibrous scaffold electrospinning

The fabrication of PLA electrospun nanofibrous scaffolds (ENSs) involved electrospinning a 12.0 weight percent solution of PLA (number-average molecular weight (M_n): 60,000 Da, NatureWorks) in chloroform and dimethylformamide (DMF) (4:1, volume ratio) solution (Merck, Germany) using a 27-gauge stainless steel needle, a tip-collector distance of 15 cm, a flow rate of 0.5 mL/h, a high voltage of 27 kV, and a drum speed of 1000 r/min. The high voltage used in the electrospinning technique caused the solution to leave the needle tip and accumulate as nanofibers on the aluminum foil surrounding the rotational shaft. The prepared scaffolds were then allowed to dry overnight in a vacuum.

Oxygen plasma treatment of scaffolds

To activate the PLA scaffold surfaces, oxygen plasma treatment was employed (plasma device Diener ZEPTO, Germany). This process was used to create peroxide groups and free radicals and to impart hydrophilic properties to the scaffolds. To perform the procedure, the clean substrates were carefully positioned on a glass plate in an oxygen plasma chamber. Various output powers (35, 65, and 95 W) and a pressure of 40 Pa at 60 s were used during the treatment. The parameters were optimized on the basis of the 2,2-diphenyl-1-picrylhydrazyl (DPPH) assay (described below) results and used for the remaining sheets.

DPPH assay

The density of the peroxide group after plasma treatment of the ENSs was assessed using the DPPH assay. Sheets were cut into equally sized pieces and immersed in DPPH (Sigma-Aldrich, USA) solution (1×10^{-4} mol/L) prepared in methanol. Samples were maintained for 1 h in the dark at room temperature, after which the consumption of DPPH molecules was calculated from the difference in the absorbance intensities (at 517 nm) between the control and plasma samples using a microplate reader (STAT FAX 2100, USA).

Graft polymerization of acrylic acid (AA)

After being removed from the plasma instrument, the samples were dipped into a solution of AA (2.5%, 5%, and 10% (volume fraction); Sigma-Aldrich, USA). The grafting reaction was accomplished by placing ampoules in a nitrogen-purged water bath at 60 °C for 4 h. The samples were then washed in deionized water at 60 °C in a water bath to remove the unreacted AA monomers and the poly(acrylic acid) that was not covalently bound to the surface. The sheets were then dried under vacuum at room temperature.

Attenuated total reflectance- Fourier transform infrared (ATR-FTIR) spectroscopy

ATR-FTIR is a reliable method for analyzing the chemical composition of materials and has been extensively used to investigate changes in chemical structures, such as the formation of new bonds that occur after polymerization. Consequently, we applied this method using a Nicolet ATR-FTIR (NEXUS 670) spectrometer to verify the graft copolymerization and record the infrared spectra of the AA and PLA/AA nanofibers.

Toluidine blue O (TBO) analysis

To estimate the number of carboxyl groups represented on the surface of the PLA/AA samples, TBO analysis was performed. To generate the ionic complex between the COO^- groups and the cationic dye, samples were immersed in TBO (Sigma-Aldrich, USA) solution (0.5 mmol/L, pH 10) for 12 h at room temperature. The scaffolds were then washed with NaOH (0.1 mmol/L) to remove unbonded TBO molecules. To desorb the bonded TBO molecules, the samples were incubated in 50% (volume fraction) acetic acid solution for 20 min on an orbital shaker. The absorbances of the samples were recorded at 623 nm using a microplate reader (STAT FAX 2100, USA). Three independent experiments were performed for each sample. TBO/50% acetic acid solution was used to calibrate the measurements under identical conditions as those of the PLA/AA samples.

Li-loading content

To produce Li-loaded PLA nanofibers (PLA/AA/Li), the sterilized grafted scaffolds were soaked in LiCl solution (10 mol/L, pH 7.00; Merck, Germany) for 5 h at room temperature, after which they were rinsed with distilled water. The amount of Li loaded onto the nanofiber samples was assessed using inductively coupled plasma mass spectrometry (ICPMS, Elan6000 DRC, Perkin Elmer, USA). In brief, Li-loaded nanofibers (1 cm^2) were immersed in a 3 mol/L KOH aqueous solution in a 50 °C oven to hydrolyze the nanofibers and resolubilize the Li ions. Then, ICPMS was used to quantify the Li concentration in the solution, followed by measurement of the loading content of Li encapsulated in the nanofibers using the following formula:

$$\text{Loading content of Lithium ion} = \frac{\text{Weight of loaded Lithium ion}}{\text{Surface area of the nanofibers}} \times 100\%.$$

Li release assay

Li released from the ENSs was assessed using ICPMS. Li-loaded samples (1 cm^2) were immersed in 1 mL of PBS and incubated at 37 °C for 2 weeks. One milliliter of the supernatant was collected at different time points (Fig. 2d shown later) and replaced with fresh PBS. PBS was used as blank, and three independent experiments were performed for each sample.

Scanning electron microscopy (SEM)

The structure and morphology of the prepared nanofibrous scaffolds were investigated using field emission SEM (FESEM MIRA3, CZ) at an accelerating voltage of 15 kV. To improve the conductivity and image acquisition, a thin gold layer was evaporated on the observing surface using a sputtering instrument (DST1-2, Nanostructured Coatings Co., Iran). The average diameter of the fibers in all SEM images of the samples was calculated using the diameter measurements from at least 100 randomly selected images using ImageJ software.

Cell seeding

For cell seeding, the scaffolds were punched in a circular form according to the sizes of the required tissue culture plates (TCPs). The scaffolds were then sterilized and incubated in DMEM supplemented with 10% FBS, 1% GlutaMAX™-I, and 1% penicillin/streptomycin. Incubation was performed overnight in a humidified incubator at 37 °C and 5% CO_2. The seeding densities were 1×10^4–2×10^4 cells/cm^2 for the adhesion, viability, and proliferation assays, and 1×10^5–2×10^5 cells/cm^2 for the differentiation assay.

Adhesion assay

The morphology and adhesion of hADMSCs and spheroids on the scaffolds were evaluated under SEM at 1, 4, and 7 d after seeding. The cell-loaded scaffolds were rinsed with PBS, fixed in 2.5% (volume fraction) glutaraldehyde (Sigma-Aldrich, USA) for 2 h, dehydrated in a graded series of alcohols, dried, and coated with a thin layer of gold for the FESEM studies [37].

Viability assay

The viability of the hADMSCs on the scaffolds was examined by dual acridine orange/ethidium bromide (AO/EB) fluorescent staining. The cell seeding process was carried out as explained above. After culture for 1, 4, and 7 d, the supernatant was removed, and a dual fluorescent staining solution containing 100 μg/mL AO and 100 μg/mL EB (Sigma, USA) was added to each well. Live and dead cells were visualized under a fluorescence microscope (Zeiss inverted fluorescence microscope, Germany). Dual AO/EB staining was performed at least in triplicate.

Proliferation assay

To evaluate the proliferation of hADMSCs on the scaffolds, the cells were seeded on sterilized nanofibrous scaffolds in 24-well TCPs, and the plates were incubated for 1, 4, and 7 d. The proliferation was assessed using the 3-(4,5-dimethylthiazol-2-yl)-2,5-diphenyltetrazolium bromide (MTT) assay, as explained previously [38]. The same protocol was also performed to evaluate the cytotoxicity (half maximal inhibitory concentration (IC_{50})) of LiCl.

In vivo experiments

Surgical procedures

Adult male Wistar rats weighing 200–250 g were maintained under standard conditions for feeding, light, temperature, humidity, and ventilation. Anesthesia, surgery, and postoperative management of the rats were performed as previously described [1]. Euthanasia of the rats was performed using an anesthetic overdose (Intraperitoneal (i.p.) injection of a combined ketamine and xylazine solution), according to the American Veterinary Medical Association guidelines. Figure 6a (shown later) shows the exposed and crushed sciatic nerve and the implanted ENS at the site of injury. The rats were randomly divided into five groups: 1) control (CTR), in which the sciatic nerves were exposed and crushed without any treatment or implantation; 2) PLA/plasma, in which crush injury was performed and the plasma-treated ENSs were implanted at the injured site and wrapped around the nerve without suturing; 3) PLA/AA, in which the plasma-treated and AA-grafted ENSs were implanted; 4) PLA/AA/Li, in which the plasma-treated and AA-grafted ENSs containing Li were implanted; and 5) PLA/AA/Li/cell, in which the plasma-treated and AA-grafted ENSs containing Li seeded with SCLCs (on Day 8 of differentiation) were implanted. All surgeries were performed by the same surgeon. The maintenance of the original positions of the scaffolds in all ENS-implanted groups was verified after 6 weeks.

Behavioral analysis of the regenerated sciatic nerve

The recovery of the sensory and motor functions of the animals' hind limbs was evaluated at 0-, 2-, 4-, and 6-week postsurgery. Using the manual von Frey filament test, the improved sensory function and mechanical sensitivity were evaluated by measuring the paw withdrawal thresholds at 0, 2, 4, and 6 weeks (0.008–300 g; TouchTest, USA), as described previously [39]. Responses to thermal stimuli were examined using a 52.5 ℃ hotplate (Borj Sanat Azma, Iran). Animals were placed on the surface one at a time, and the reaction time (in seconds) until licking the hind paw or jumping was recorded; at which time, the animal was immediately removed from the hotplate [40]. The heat stimulation cutoff time was 30 s.

To measure the amount of motor function recovery, the CatWalk gait test was performed at weeks 0, 2, 4, and 6 after injury. Walking track analysis was performed by calculating the sciatic function index (SFI) from the gait patterns of the animals in accordance with the following formula [39]:

$$\mathrm{SFI} = -38.3 \times \frac{\mathrm{EPL} - \mathrm{NPL}}{\mathrm{NPL}} + 109.5 \times \frac{\mathrm{ETS} - \mathrm{NTS}}{\mathrm{NTS}} + 13.3 \times \frac{\mathrm{EITS} - \mathrm{NITS}}{\mathrm{NITS}} - 8.8,$$

where NPL is the normal print length, EPL is the experimental print length, NTS is the normal toe spread, ETS is the experimental toe spread, NITS is the normal intertoe spread, and EITS is the experimental intertoe spread.

Finally, a narrow run track with a width of 12 cm, a height of 15 cm, and a length of 45 cm covered by white paper was used. To record the footprints of the rats, they were allowed to move in one direction only with their hind paws dipped in water-soluble inks (red for the injured and green for the intact hind paw).

Muscle weight ratio evaluation

To further assess the functional recovery of the sciatic nerve, the wet weight of the gastrocnemius muscles was measured as an index of atrophy induced by denervation of the affected muscle. To perform this evaluation, the connective tissue surrounding the nerve was removed, and the wet weight of the gastrocnemius muscle was determined 6 weeks after surgery using the following formula [41]:

$$\text{Wet weight ratio} = \frac{\text{Weight of surgery gastrocnemius}}{\text{Weight of contralateral gastrocnemius}} \times 100\%.$$

Electrophysiological analysis of the regenerated sciatic nerve

Electrophysiological analysis was performed 6 weeks after surgery. To investigate the compound muscle action potential (CMAP) and terminal latency (TL), animals were anesthetized [1, 42], after which a bipolar stimulating electrode (with a standard subdermal needle) and a recording electrode were placed on the proximal portion of the exposed injured sciatic nerve trunk and the belly of the gastrocnemius muscle, respectively. The stimulating mode was set to pulse mode for a duration of 0.2 ms and the stimulus intensity of 1.0 mA. To determine the nerve conduction velocity (NCV), two different points on either side of the crush-injured site were carefully chosen. The CMAP, NCV, and TL were detected in a blinded fashion and measured using PowerLab devices and software (AD Instruments, Australia).

Histological analysis of the regenerated sciatic nerve

To perform hematoxylin and eosin (H&E) staining of the sciatic nerves, the animals were sacrificed 6 weeks after the surgery, the time when the repair had also taken place. The harvested sciatic nerves were fixed in 10% (volume fraction) neutral buffered formalin (pH 7.26) for 48 h, processed and embedded in paraffin, sectioned to 5-μm thicknesses, and stained with H&E. Finally, the histological slides were examined under light microscopy (Olympus BX51, Japan).

To localize the expression of S100B, NF200, and SOX10, immunohistochemistry was performed on the paraffin transverse sections of the crushed nerves as described previously [43]. The primary antibodies were monoclonal mouse anti-S100B (1:200, volume ratio), mouse anti-NF200 (1:300, volume ratio), and mouse anti-Sox10 (1:200, volume ratio) (all from Millipore, USA). Slides were developed using the LSAB kit (DAKO), visualized using diaminobenzidine (DAB), and analyzed using a Zeiss Axioplan 2 imaging microscope.

To monitor the internal tissue architecture, toluidine blue staining and transmission electron microscopy (TEM) analysis were performed in the CTR, PLA/AA/Li, and PLA/AA/Li/cell groups. The crushed area was harvested and fixed using 2.5% glutaraldehyde, 1% (0.01 g/mL) osmium tetroxide, and 0.5% (5 g/L) uranyl acetate solution, dehydrated in ethanol, and impregnated with 100% epoxy resin.

For toluidine blue staining, samples were cut into semi-thin (1 μm) sections at the midpoint of the crushed area. Then, the sections were stained with toluidine blue to label the myelin sheath and examined under a light microscope (Zeiss inverted fluorescence microscope, Germany). Ten random fields were selected from each section, and the axon density (axons/mm^2), axon diameter, and G-ratio (axon diameter/fiber diameter) were analyzed using ImageJ software.

For TEM, samples were epoxy resin-embedded and sectioned (80 nm) at the midpoint of the crushed area, stained with 2% uranyl acetate for approximately 30 min at room temperature, followed by staining with citric acid for 15 min at room temperature, and examined using a transmission electron microscope (PHILIPS, EM208S, 100 kV, Netherland).

Statistics

All data were presented as mean ± standard deviation (SD) ($n \geq 3$). To evaluate statistically significant differences between the groups, the one-way analysis of variance (ANOVA) was employed followed by post hoc Student's t and Tukey–Kramer tests. p values less than 0.05 were considered statistically significant. All statistical analyses were performed using Graphpad Prism software.

Results

Characterization of hADMSCs

The isolated hADMSCs were characterized using flow cytometry. Our results showed that these cells were positive for mesenchymal CD markers, including CD73, CD90, and CD105 (99.7%, 99.4%, and 100%, respectively), but negative for the hematopoietic stem cell marker CD45 (0.304%) (Fig. S1 in Supplementary Information). In addition, the mesenchymal characteristics of these cells were verified through the analysis of their differentiation potentials toward chondrogenic, adipogenic, and osteogenic lineages (Fig. S2 in Supplementary Information).

Differentiation of hADMSCs into SCLCs

The morphological characteristics of Schwann cells, including the bipolar and tripolar morphologies (Fig. 1a), were observed after the expansion of cells from spheroids (Figs. 1a4 and 1a5). To evaluate Schwann cell differentiation of hADMSCs, the expression of Schwann cell markers was examined using real-time reverse transcription (RT)-PCR after 14 d of culture. Our results showed that the expression levels of *S100B*, myelin basic protein (*MBP*), *GAP43*,

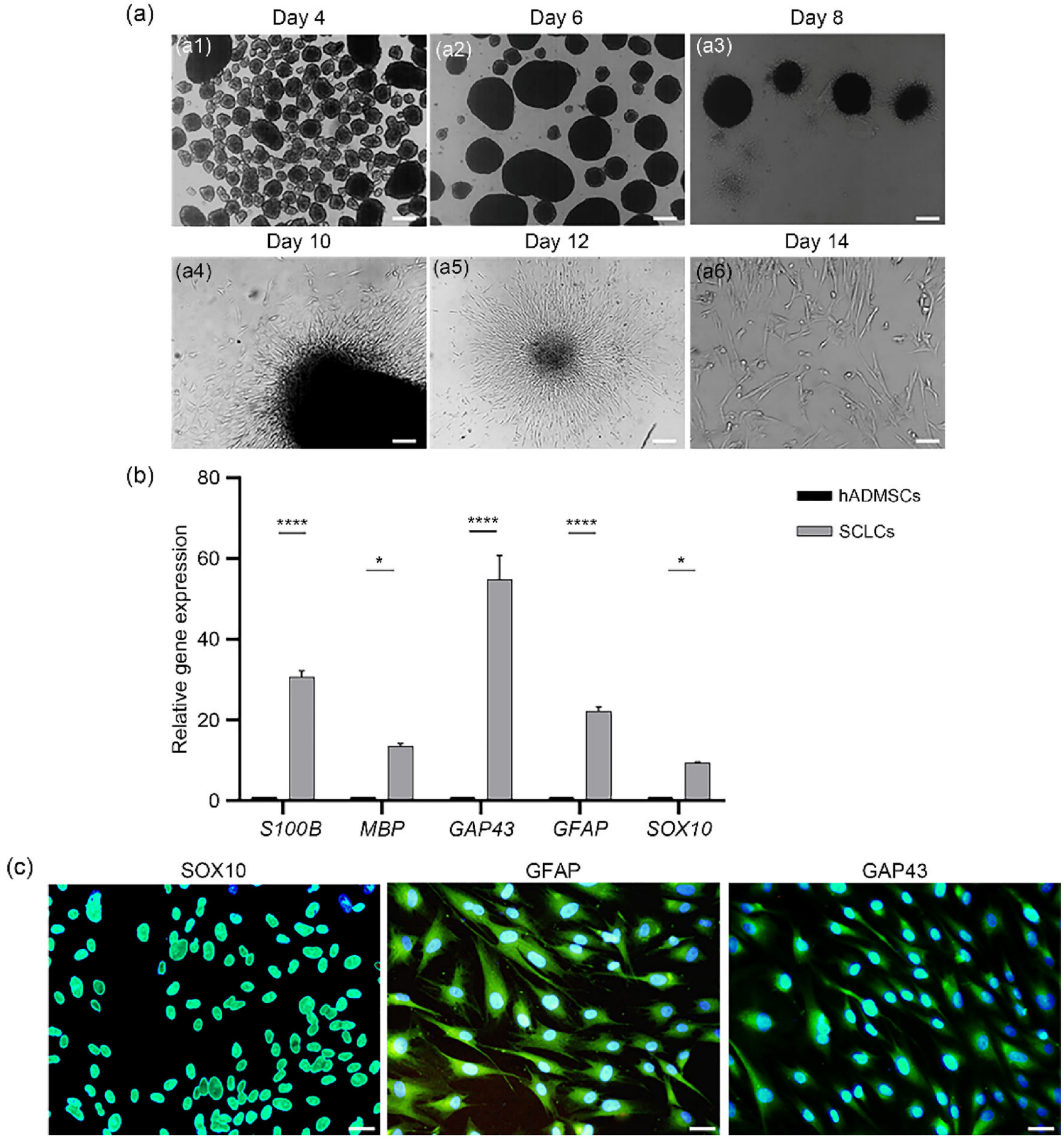

Fig. 1 Differentiation of human adipose-derived mesenchymal stem cells (hADMSCs) into Schwann cell-like cells (SCLCs). **a** Phase contrast images of Schwann cell differentiation. hADMSCs were cultured in pre-inducing medium on a nonadhesive plate for 7 d (a1, a2), followed by the addition of Schwann cell inducing medium on an adhesive plate for a further 7 d (a3–a6). Note the spheroid formation in (a1) and (a2), cell migration in (a4) and (a5), and expansion and differentiation of SCLCs in (a6). Scale bars: 200 μm (a1, a2, a3, and a5), 150 μm (a4), 100 μm (a6). **b** Real-time reverse transcription-polymerase chain reaction (RT-PCR) analysis of the expression of Schwann cell markers in hADMSCs after 14 d of culture. The expression of all genes was significantly upregulated in cells cultured in Schwann cell inducing medium compared with the control group. **c** Immunofluorescence staining of hADMSCs after 14 d of culture with anti-SOX10, anti-GFAP, and anti-GAP43 antibodies. All nuclei were stained with 4’,6-diamidino-2-phenylindole (DAPI). Nuclear expression of SOX10 and cytoplasmic expression of GFAP and GAP43 can be observed in induced hADMSCs. Scale bar: 100 μm. All data are expressed as mean ± standard deviation (SD), $n = 5$. $^{*}p < 0.05$, $^{****}p < 0.0001$, one-way analysis of variance (ANOVA) with Tukey–Kramer test. MBP: myelin basic protein; GAP43: growth associated protein 43; GFAP: glial fibrillary acidic protein; SOX10: SRY-box transcription factor 10

GFAP, and *SOX10* were significantly upregulated (30.69 ± 0.87, 13.40 ± 0.48, 54.75 ± 3.50, 22.16 ± 0.65, and 9.42 ± 0.17 times, respectively) in the induced cells compared with the control group (Fig. 1b). An even more significant expression level of these genes was observed when the cells were cultured under three-dimensional (3D) conditions (on PLA/plasma ENSs) compared with two-dimensional (2D) conditions (on TCP) (Fig. S3 in Supplementary Information). The significant expression of Schwann cell markers (GFAP, SOX10, and GAP43) in the induced cells was also confirmed by immunofluorescence analysis (Fig. 1c), indicating that our differentiation protocol efficiently induces the differentiation of hADMSCs into SCLCs.

Characterization of electrospun nanofibrous scaffolds

Various output powers (35, 65, and 95 W) and a pressure of 40 Pa were used to perform plasma surface activation for 60 s. Evaluation of the peroxide group densities in these three groups was performed using the DPPH assay. Figure 2a clearly illustrates the significant differences in DPPH absorption among the treated samples. Notably, the DPPH absorption in the 65-W treated samples (14.54 ± 0.32) was significantly higher than that in the 35-W (10.32 ± 0.39, $p = 0.0003$) and 95-W (12.78 ± 0.29, $p = 0.0255$) treated groups. Consequently, the 65-W samples exhibited higher peroxide group densities than the other groups, thus allowing further investigations.

As shown in Fig. 2b, the ATR-FTIR test was used to assess the surface chemistry of the acrylic acid-modified nanofibers. The characteristic peak in the PLA spectrum at 1752 cm^{-1} was attributed to the stretching vibrations of $\text{C}=\text{O}$. Furthermore, the C–O bond in the $\text{–O–C}=\text{O}$ group was responsible for the peaks at 1050, 1086, and 1131 cm^{-1}. The twin peak at around 1379 cm^{-1} (–CH– bending vibrations), the sharp peak at 1182 cm^{-1} (C–O bond), and the peak at 1449 cm^{-1} (–CH_3 vibrations) were all related to the PLA structure and appeared in the PLA/AA nanofibers [44]. The PLA peaks were all repeated in the PLA/AA spectrum, but this sample had higher intensity absorption at 1752 cm^{-1}, corresponding to the carbonyl group. In addition, a peak was observed at 1712 cm^{-1}, corresponding to the carboxylic acid group of polyacrylic acid [45].

The concentration of carboxyl groups was evaluated by TBO assay after AA graft polymerization (Fig. 2c). Our results showed that an increase in the monomer concentration from 2.5% (0.025 g/mL) to 10% (0.1 g/mL) resulted in a significant increase in the COOH density and surface active sites for loading Li.

Because we used Li (a glycogen synthase kinase 3β (GSK3β) inhibitor) to mimic the Wnt/β-catenin signaling pathway, the Li release profile from the nanofibrous scaffolds was analyzed using the ICPMS assay. The maximum Li concentrations released from PLA, PLA/plasma, PLA/2.5% AA, PLA/5% AA, and PLA/10% AA were (0.48 ± 0.10), (0.96 ± 0.10), (1.95 ± 0.10), (2.91 ± 0.10), and (3.64 ± 0.10) mmol/L, respectively. The duration of ion release for PLA, PLA/plasma, PLA/2.5% AA, PLA/5% AA, and PLA/10% AA was approximately 48, 72, 120, 168, and 264 h, respectively (Figs. 2d and 2e).

Previous studies have demonstrated that Li concentrations below 10 mmol/L are not toxic [24]. Using the MTT assay, we found that the inhibitory concentration (IC_{50}) of Li for hADMSCs was approximately 10 mmol/L, indicating that none of the Li concentrations released from the scaffolds over 7 d were toxic (Fig. 2f). Furthermore, we demonstrated that the concentrations of Li released from the PLA/AA/Li ENSs (0.02 to (3.64 ± 0.10) mmol/L) were within the range of concentrations that upregulated Wnt/β-catenin target genes (*cyclinD1* and *c-Myc*) (Fig. 2g).

Our analysis of 10% AA-grafted ENSs showed that Li ions could be detected in the media until 11 d (264 h) (Figs. 2d and 2e), suggesting that this scaffold had the highest Li-loading content ((0.0200 ± 0.0003) mg/cms) compared with the other samples (Fig. 2h). Therefore, we selected PLA/10% AA (hereafter will be referred to as PLA/AA/Li) for the next steps.

Morphological observations of electrospun nanofibrous scaffolds

The nanofibrous structure was investigated under SEM. As shown in Fig. 3, all ENSs had a bead-free nanofibrous structure with interconnected pores. Image analysis of the nanofibers showed a mean diameter of (558 ± 12) nm for virgin PLA and (555 ± 11) nm for PLA/plasma nanofibers. No significant differences were noted between the surface morphologies of the nanofibers, porosities, or fiber sizes before and after plasma surface activation, graft polymerization of AA, or ion-exchange procedure.

hADMSC adhesion, viability, and proliferation on electrospun nanofibrous scaffolds

To examine the morphology, adhesion, and spreading of cells and spheres on different scaffolds, hADMSCs or spheroids were cultured on the scaffolds for 1, 4, and 7 d. Our SEM micrographs revealed the attachment and spreading of both spheroids and cells on all scaffolds (Figs. 3b and 3c).

The AO/EB dual staining showed no significant apoptosis by any of the scaffolds (data of PLA/10% AA have been shown). Single-cell counting revealed viabilities of (97.66 ± 1.52)%, (97.66 ± 0.57)%, and (98.33 ± 1.15)% at Days 1, 4, and 7 for cultured hADMSCs on PLA/10% AA ENSs

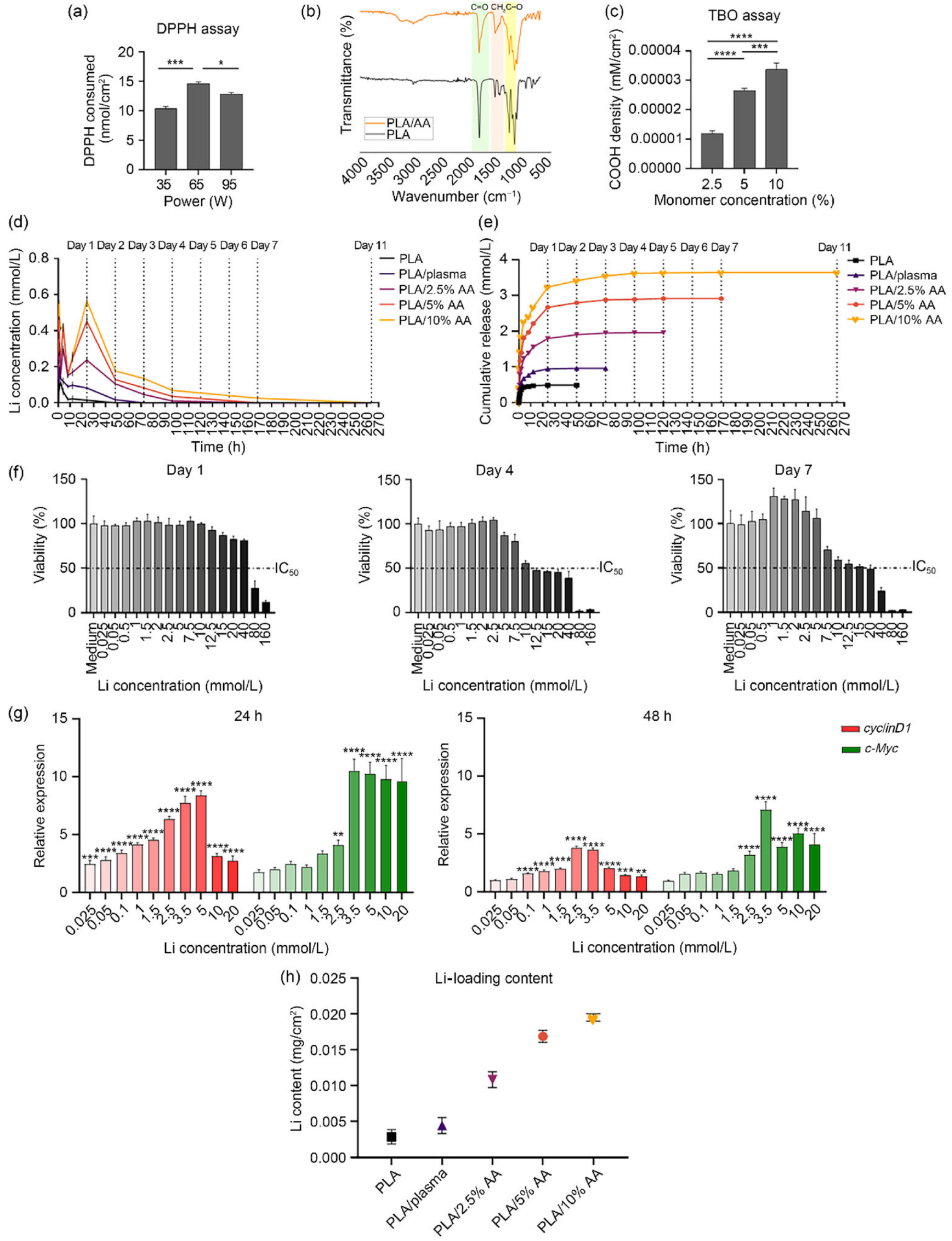

Fig. 2 Characterization of electrospun nanofibrous scaffolds (ENSs). **a** 2,2-Diphenyl-1-picrylhydrazyl (DPPH) absorption in ENSs activated with plasma at different output powers. The DPPH absorption of 65-W samples was significantly higher than those of 35-W and 95-W samples. The samples were prepared in triplicate. **b** Attenuated total reflectance Fourier transform infrared (ATR-FTIR) spectra of polylactide (PLA) and PLA/acrylic acid (AA) ENSs showing the surface chemistry of the nanofibers. **c** Carboxyl group concentration represented on the surface of PLA/AA samples after graft polymerization of AA, as evaluated by the toluidine blue O (TBO) assay. Note that enhancing the monomer concentration from 2.5% to 10% (1% = 0.01 g/mL) resulted in a significant increase in the COOH density. 1 mM = 1 mmol/L. **d** Release profile of lithium (Li) from ENSs assessed by inductively coupled plasma mass spectrometry (ICPMS) assay in phosphate-buffered saline (PBS) (pH 7.4 at 37 °C). A sustained release was observed until Day 11 (0.02 mmol/L) in the PLA/10% AA group. **e** Cumulative release profiles of Li from ENSs assessed by ICPMS assay in PBS (pH 7.4 at 37 °C). The Li concentration released from PLA/10% AA was maximally (3.64 ± 0.10) mmol/L. PLA/10% AA showed the longest period of Li release (264 h). **f** Toxic concentration of Li for human adipose-derived mesenchymal stem cells (hADMSCs) after 1, 4, and 7 d of culture using the 3-(4,5-dimethylthiazol-2-yl)-2,5-diphenyltetrazolium bromide (MTT) assay. The half maximal inhibitory concentration (IC_{50}) was approximately 10 mmol/L. **g** Expression of *cyclinD1* and *c-Myc* (Wnt/β-catenin signaling target genes) in hADMSCs cultured for 24 and 48 h in the presence of different concentrations of Li in culture media compared with those without Li. **h** Evaluation of Li-loading content between five groups of ENSs. As shown, the Li-loading content of PLA/10% AA was significantly higher than those of the other samples. All data are expressed as mean ± standard deviation (SD). $^{*}p < 0.05$, $^{**}p < 0.01$, $^{***}p < 0.001$, $^{****}p < 0.0001$, one-way analysis of variance (ANOVA) with Tukey–Kramer test

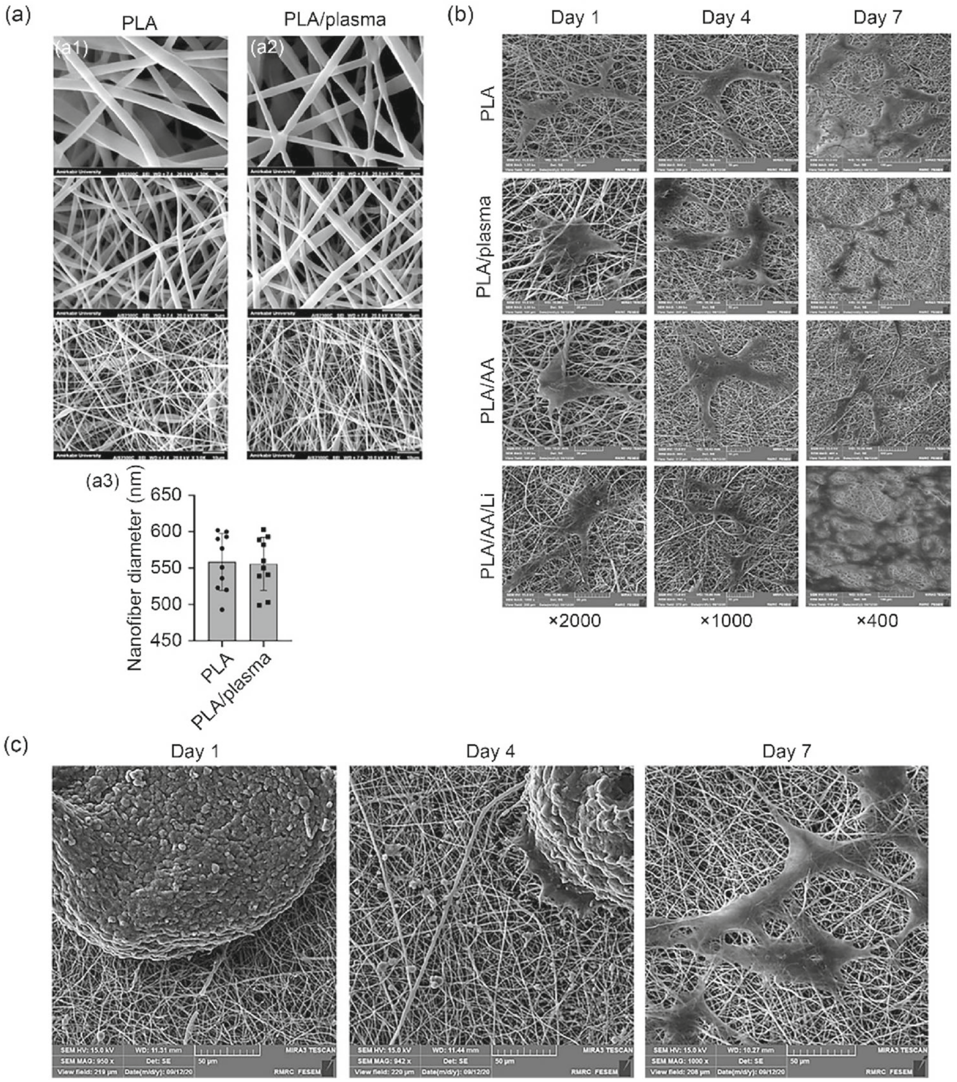

Fig. 3 Scanning electron microscopy (SEM) analysis of the fabricated polylactide (PLA) nanofibers. **a** Nanofibrous scaffolds before (a1) and after (a2) oxygen plasma surface modification. Qualitatively, no change was observed in the surface morphology of nanofibers after treatment compared with that observed before treatment. Image analyses of the nanofibers indicated a mean diameter of (558 ± 12) and (555 ± 11) nm, as seen in (a3), before and after oxygen plasma surface modification, respectively. The corresponding average diameter of the nanofibers was evaluated using ImageJ software ($n = 10$). Data are expressed as mean ± standard deviation (SD). **b** Adhesion and spreading of human adipose-derived mesenchymal stem cells (hADMSCs) on different scaffolds 1, 4, and 7 d after seeding indicated the biocompatibility of the electrospun nanofibrous scaffolds (ENSs). **c** Adhesion and spreading of spheroids on PLA/AA/Li 1, 4, and 7 d after plating indicated the biocompatibility of the ENS

($n = 10$) (Fig. 4a). Moreover, using the MTT assay, no significant difference in cell proliferation rate was observed in the hADMSCs cultured on any of the nanofibrous scaffolds compared with those in the control group (TCP) (Fig. 4b).

Together, these results showed that ENSs have a proper nanofibrous topography with a high surface area, which supports cell growth and proliferation suitable for tissue engineering.

Effects of Li-loaded scaffolds on SCLC differentiation of hADMSCs

To examine the effects of Li-loaded ENSs on SCLC differentiation of hADMSCs, the cells were cultured on different scaffolds for 14 d, followed by analysis of the expression levels of Schwann cell markers (*S100B*, *SOX10*, *GFAP*, and *GAP43*) using real-time PCR. We found that the expression of all genes was significantly increased in cells cultured on Li-loaded ENSs compared with cells cultured without Li (Fig. 5a). Consistently, immunostaining of the hADMSCs cultured on PLA/10% AA/Li (Fig. 5b) showed significant expression of SOX10, GFAP, and GAP43 ((84.66 ± 6.50)%, (84.00 ± 6.24)%, and (82.00 ± 4.58)%, respectively) compared with those without Li ((26.33 ± 5.03)%, (37.00 ± 5.29)%, and (28.33 ± 9.29)%, respectively).

The significant difference in the level of gene expression between Li-loaded and Li-free scaffolds indicated the decisive role of Li in SCLC differentiation. Because we have demonstrated that the concentrations of Li released from the PLA/AA/Li ENSs upregulated Wnt/β-catenin target genes, it is plausible to claim that Li promoted the SCLC differentiation of hADMSCs through the activation of the Wnt/β-catenin signaling pathway.

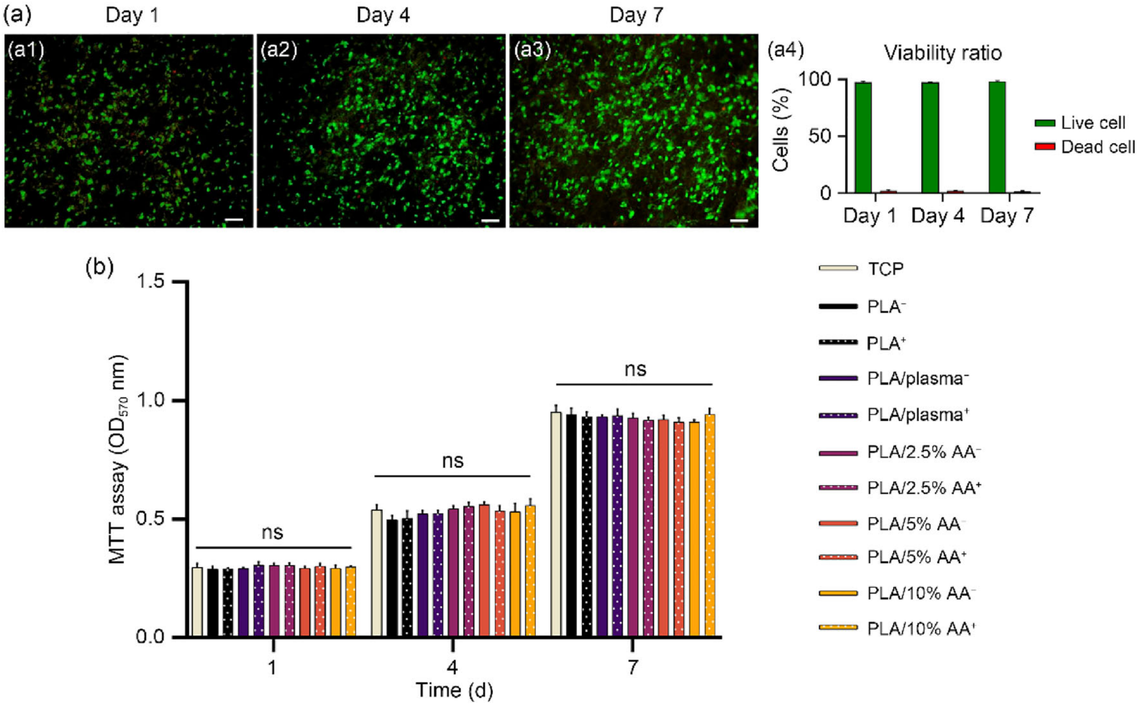

Fig. 4 Viability and proliferation of human adipose-derived mesenchymal stem cells (hADMSCs) on electrospun nanofibrous scaffolds (ENSs). **a** Live–dead assay by acridine orange/ethidium bromide (AO/EB) dual staining. Representative images show the viability of hADMSCs on PLA/10% AA^{+} ENSs. Live cells show green fluorescence and dead cells show orange-red fluorescence. Scale bars represent 200 μm (a1–a3). Viability ratio is calculated by single-cell counting 1, 4, and 7 d after culture of hADMSCs on PLA/10% AA^{+} ENSs ($n = 10$) (a4). **b** 3-(4,5-Dimethylthiazol-2-yl)-2,5-diphenyltetrazolium bromide (MTT) assay of hADMSCs on ENSs for 1, 4, and 7 d. The cell proliferation rate showed no significant differences among the groups at each time point ($n = 5$). $^{+}$ indicates the ENS with lithium (Li) and $^{-}$ indicates the ENS without Li. All data are expressed as mean ± standard deviation (SD), one-way analysis of variance (ANOVA) with the Tukey–Kramer test. OD_{570}: optical density at 570 nm; ns: not significant; TCP: tissue culture plate; PLA: polylactide; AA: acrylic acid

Effects of Li-loaded scaffolds on the recovery of sensory and motor function in a rat model of sciatic nerve injury

To determine whether the ENSs could promote regeneration and recover the function of injured peripheral nerves in vivo, we implanted our engineered scaffolds at the site of sciatic nerve injury and wrapped them around without suturing. We then performed functional, electrophysiological, and histological analyses. The Wistar rats were divided into five groups: 1) control (CTR), 2) PLA/plasma, 3) PLA/AA, 4) PLA/AA/Li, and 5) PLA/AA/Li/cell (SCLCs seeded on plasma-treated AA-grafted ENSs containing Li). Sensory and motor functional recovery of the hind limbs were assessed on Day 0 (the 1st day after surgery) and at 2, 4, and 6 weeks after surgery. Sensory-motor function was examined by analyzing the paw withdrawal threshold using the von Frey filament test. Our results showed that the thresholds in the animals in the PLA/AA/Li and PLA/AA/Li/cell groups ((8.33 ± 0.06) and (11.03 ± 0.54) g, respectively) were significantly lower than those in the CTR group ((36.83 ± 2.23) g) ($p < 0.0001$) (Fig. 6b), indicating that the sensory-motor function of the injured sciatic nerve was recovered by the implanted scaffolds.

Sensory recovery was evaluated using thermal withdrawal latency (TWL) analysis. We found that the TWL in the PLA/AA/Li and PLA/AA/Li/cell groups ((2.35 ± 0.47) and (2.33 ± 0.23) s, respectively) was significantly decreased compared with that in the CTR group ((7.93 ± 0.20) s) ($p < 0.0001$), indicating the improvement of functional sensory recovery in these groups (Fig. 6c).

Motor recovery after sciatic nerve injury was assessed using CatWalk gait analysis, which is a routine method used to examine nerve regeneration and functional recovery. This method is a helpful measure for evaluating the middle-stage recovery in muscle force 6-week postsurgery [1]. The SFI values and walking track prints of all five groups are shown in Figs. 6d and 6e, respectively. At 6-week postsurgery, the SFI (0 = normal; −100 = nonfunctional) in the PLA/AA/Li and PLA/AA/Li/cell groups (−14.35 ± 0.73 and −13.71 ± 0.81, respectively) was significantly increased compared with that in the CTR group (−41.50 ± 2.64) ($p < 0.001$). In addition, in these two groups, the footprints showed almost the same distances between the front and hind paws on a step sequence

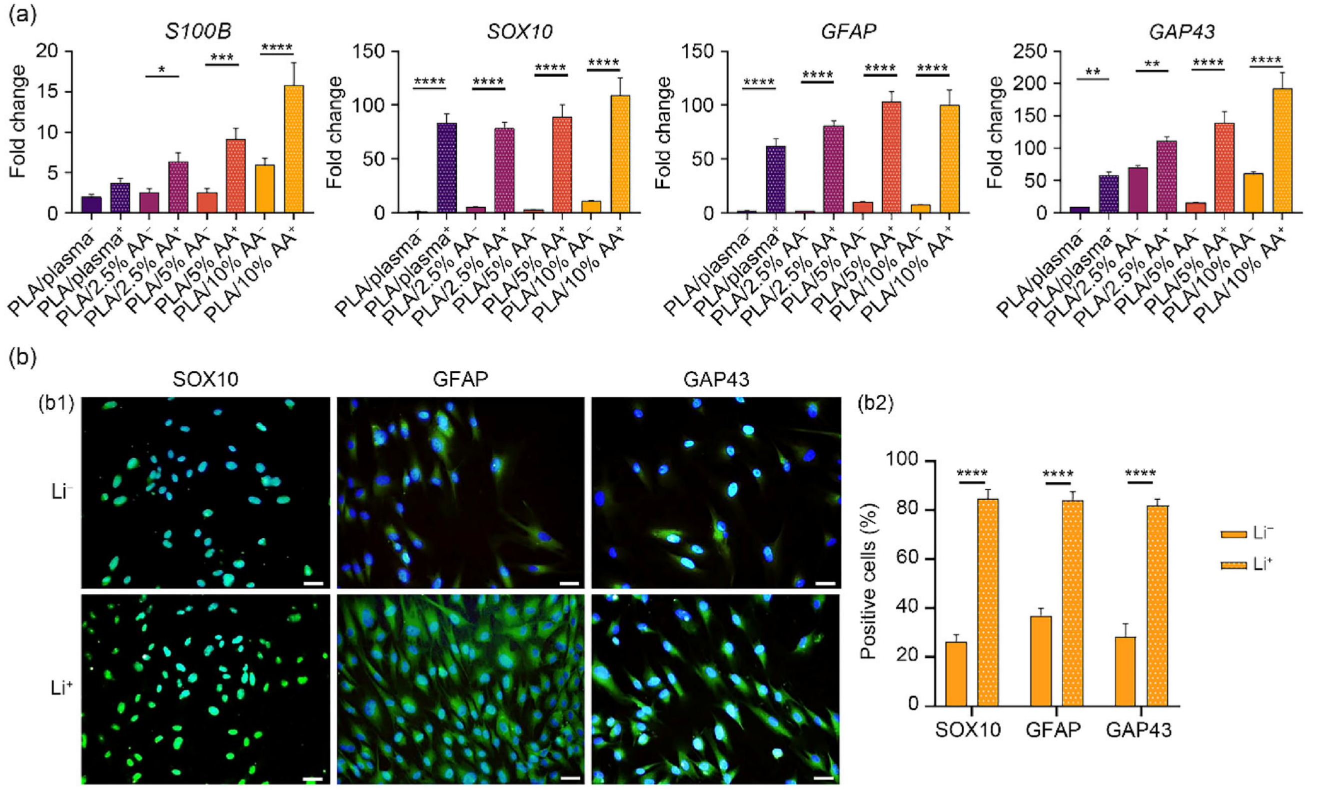

Fig. 5 Differentiation of human adipose-derived mesenchymal stem cells (hADMSCs) cultured on lithium (Li)-loaded electrospun nanofibrous scaffolds (ENSs) into Schwann cell fates. **a** Real-time reverse transcription-polymerase chain reaction (RT-PCR) analysis of the expression of Schwann cell markers in hADMSCs cultured on ENSs (with Li versus without Li) for 14 d. The expression of all genes was significantly upregulated in the Li-loaded ENSs compared with their own control group. $^+$ indicates the ENS with Li and $^-$ indicates the ENS without Li. **b** Immunofluorescence staining of hADMSCs with anti-SOX10, anti-GFAP, and anti-GAP43 after 14 d of culture on Li$^+$ (PLA/10% AA ENS containing Li) versus Li$^-$ (PLA/10% AA ENS without Li). All nuclei were stained with DAPI. Nuclear expression of SOX10 and cytoplasmic expression of GFAP and GAP43 were observed in the induced hADMSCs. Scale bars represent 100 µm (b1). Comparative analysis of the mean percentages of SOX10, GFAP, and GAP43 markers (n = 10) (b2). All data are expressed as mean ± standard deviation (SD). $^*p < 0.05$, $^{**}p < 0.01$, $^{***}p < 0.001$, $^{****}p < 0.0001$, one-way analysis of variance (ANOVA) with Tukey–Kramer test. GFAP: glial fibrillary acidic protein; GAP43: recombinant growth associated protein 43; PLA: polylactide; AA: acrylic acid; DAPI: 4’,6-diamidino-2-phenylindole

and were improved significantly compared with those in the CTR group (Fig. 6e). These findings imply that motor function was recovered in the Li-loaded groups.

To evaluate muscle atrophy, the gastrocnemius muscles from both the injured and the contralateral sides were dissected 6-week postsurgery and their wet weights were measured. Morphological observation showed that the gastrocnemius muscles on the injured side were atrophied in all groups (Fig. 7a). However, in the PLA/plasma and PLA/AA groups, the wet muscle weights of the gastrocnemius (injured side/intact side) were significantly higher ((61.83 ± 1.59)% and (67.51 ± 1.15)%, respectively) compared with the CTR group ((53.44 ± 0.57)%) ($p < 0.01, p < 0.0001$). Interestingly, in the PLA/AA/Li and PLA/AA/Li/cell groups, the wet muscle weights were significantly higher than that of the CTR group ((81.66 ± 1.66)% and (83.32 ± 0.78)%, respectively) and reflected 80% of the muscle weight of the intact side ($p < 0.0001$) (Fig. 7b).

These findings suggest that PLA/AA/Li and PLA/AA/Li/cell implantation improves the recovery of sensory, motor, and sensory-motor abilities after sciatic nerve injury. The results also indicate that ENSs do not disrupt the normal function of the sciatic nerve and are therefore harmless to the peripheral nerve tissue.

Li-loaded scaffolds recovered the CMAP, NCV, and TL in a rat model of sciatic nerve injury

To evaluate the functional regeneration and muscle reinnervation of the injured nerve, electrophysiological parameters were assessed 6-week postsurgery. As shown in Figs. 7c–7e and Fig. S5 (Supplementary Information), the CMAP or NCV in the PLA/plasma and PLA/AA groups did not change significantly compared with that in the CTR group. However, the CMAP and NCV in the PLA/AA/Li ((25.84 ± 0.17) mV and (54.37 ± 2.51) m/s, respectively) and PLA/AA/Li/cell

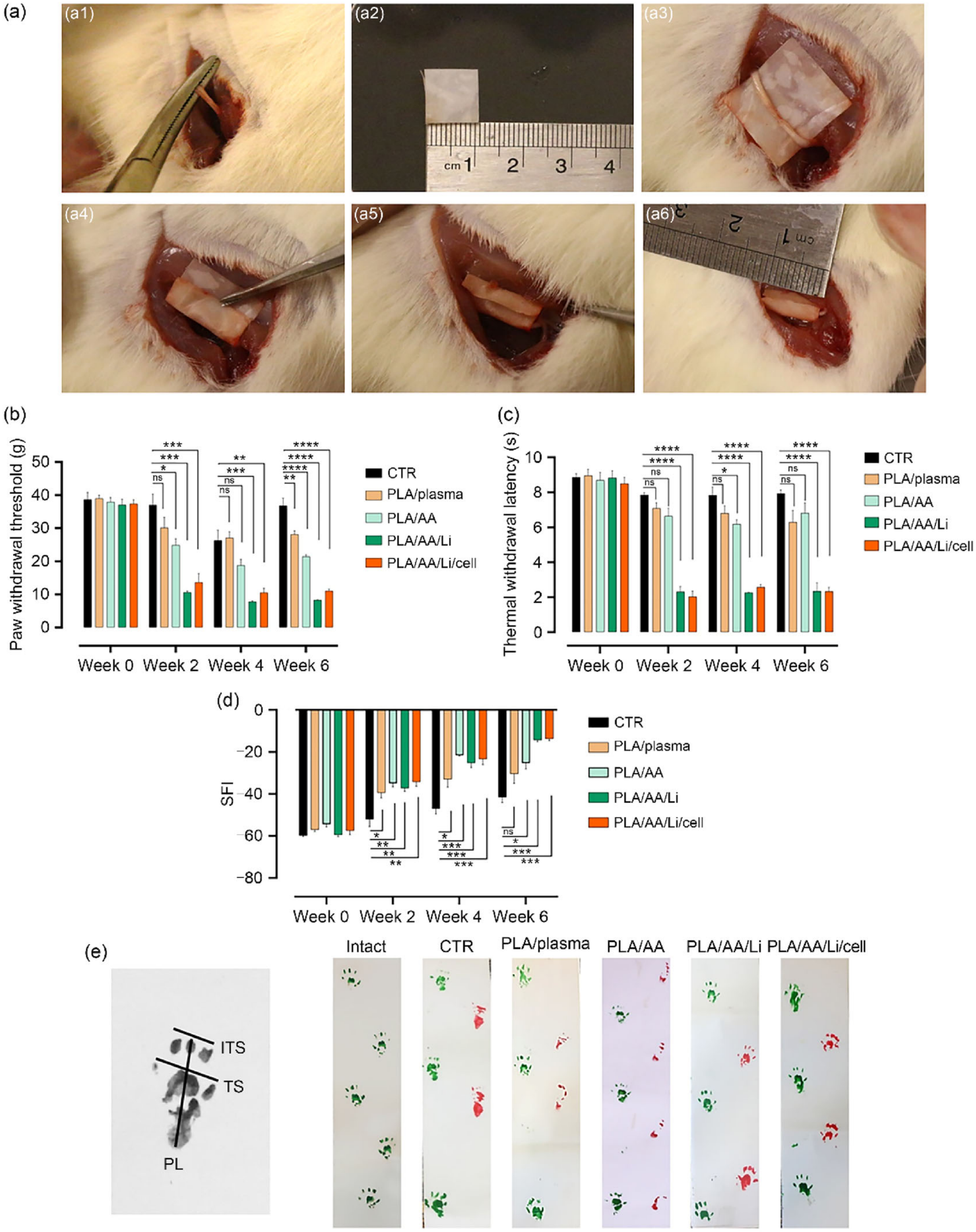

Fig. 6 Recovery analysis of sensory and motor function in the peripheral nerve injury (PNI) rat model. **a** Wistar rats were anesthetized by intraperitoneal injection of ketamine and xylazine HCl, and the sciatic nerve was exposed and then crushed (a1). The ENS (a2) was implanted at the injury site (a3) and wrapped around the nerve (a4–a6). **b**–**d** Sensory and motor functional recovery of animals' hind limbs in different groups was assessed 0- (the 2nd day after surgery), 2-, 4-, and 6-week postsurgery using von Frey filament (**b**), thermal withdrawal latency (TWL) (**c**), and walk gait analysis (**d**). **b** The von Frey results showed that the paw withdrawal threshold in the control (CTR) group was significantly higher than that in the lithium (Li) and Li/cell-treated groups. **c** Hot plate results showed that the TWLs of the Li and Li/cell groups were significantly reduced compared with that of the CTR group, indicating functional sensory recovery in these groups. **d** The sciatic function index (SFI) values in the PLA/AA/Li and PLA/AA/Li/cell groups were increased significantly compared with that of the CTR group 6-week postsurgery. **e** Progression of walking tracks (footprints) in the normal and treated groups 6-week postsurgery. In the PLA/AA/Li and PLA/AA/Li/cell groups, the footprints showed almost the same distances and were improved significantly compared with the CTR group. All data are expressed as mean ± standard deviation (SD), $n = 5$. $^{*}p < 0.05$, $^{**}p < 0.01$, $^{***}p < 0.001$, $^{****}p < 0.0001$, one-way analysis of variance (ANOVA) with Tukey–Kramer test. PLA: polylactide; AA: acrylic acid; PL: print length (length from the third toe to the heel); TS: toe spread (length from the first to the fifth toe); ITS: intertoe spread (length from the second to the fourth toe); ns: not significant

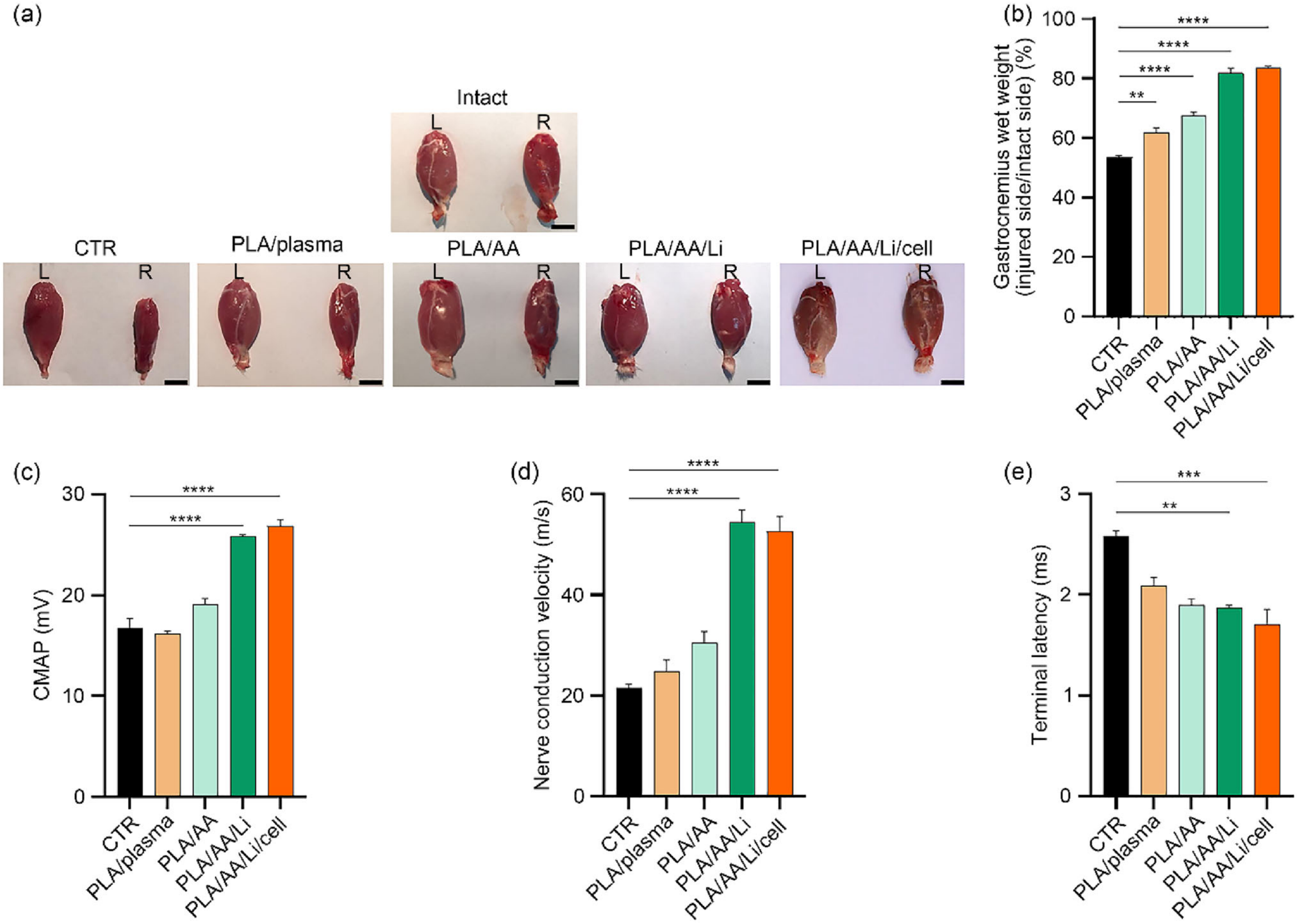

Fig. 7 Musculus gastrocnemius evaluation and electrophysiological assessment in the peripheral nerve injury (PNI) rat model. **a** Representative gross appearance of the gastrocnemius muscles from both hind limbs 6-week postsurgery in the different groups. Although the muscles on the injured side were atrophied in all groups, the muscle size and morphology in the PLA/AA/Li and PLA/AA/Li/cell groups were more similar to those on the intact side than those in the other groups. Scale bars represent 10 mm. L: left (intact) side; R: right (injured) side. **b** The wet weights of the gastrocnemius muscle in all groups, especially in the PLA/AA/Li and PLA/AA/Li/cell groups, were increased significantly compared with that of the control (CTR) group. **c**–**e** Quantitative analyses of the electrophysiological assessment record at 6-week postsurgery. The injured nerves in the PLA/AA/Li and PLA/AA/Li/cell groups were significantly recovered in terms of the compound muscle action potential (CMAP) (**c**), nerve conduction velocity (NCV) (**d**), and terminal latency (TL) (**e**) compared with those in the CTR group. All data are expressed as mean ± standard deviation (SD), $n = 5$. $^{**}p < 0.01$, $^{***}p < 0.001$, $^{****}p < 0.0001$, one-way analysis of variance (ANOVA) with Tukey–Kramer test. PLA: polylactide; AA: acrylic acid; Li: lithium

groups ((26.86 ± 0.65) mV and (52.56 ± 3.03) m/s, respectively) were significantly increased compared with those in the CTR group ((16.77 ± 0.91) mV and (21.42 ± 0.86) m/s, respectively). The TL was significantly decreased in the PLA/AA/Li and PLA/AA/Li/cell groups ((1.86 ± 0.03) and (1.70 ± 0.15) ms, respectively) compared with that in the CTR group ((2.58 ± 0.04) ms). These results clearly indicated that PLA/AA/Li and PLA/AA/Li/cell implantation enhanced nerve regeneration after sciatic nerve injury.

Li-loaded scaffolds increased the number of organized regenerating axons in a rat model of sciatic nerve injury

For histological evaluation of the regenerated sciatic nerve, H&E staining was performed 6 weeks after surgery. As shown in Fig. S4 (Supplementary Information), in the intact group, myelinated fibers were well arranged with no signs of nerve damage. However, in the CTR group, there was loss of myelinated axons in the injured area, which was filled by fibrous connective tissues (Fig. 8a). In the PLA/plasma and PLA/AA groups, disorganized nerve fibers were surrounded

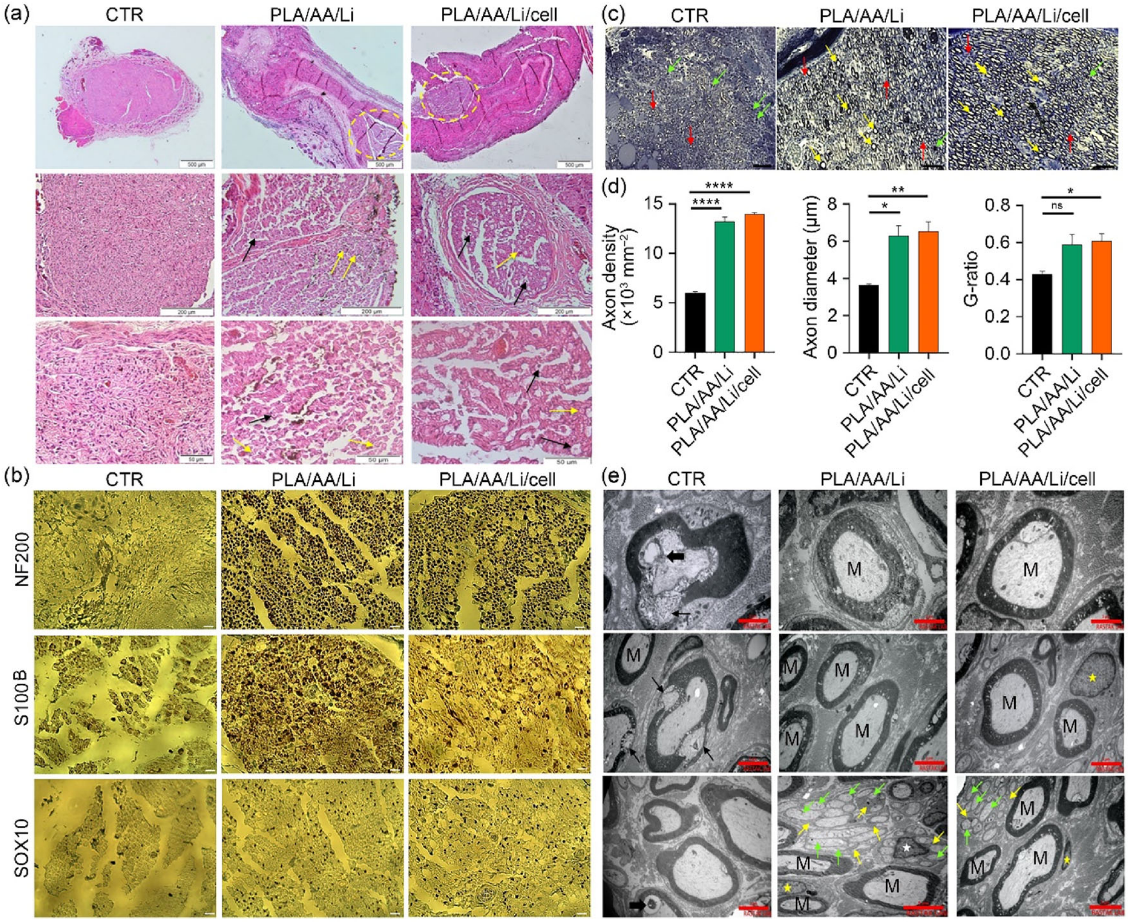

Fig. 8 Histological analysis of the regenerated sciatic nerve in the peripheral nerve injury (PNI) rat model. **a** Histopathology of the sciatic nerves 6 weeks after injury indicated more arranged fibers and regeneration of the myelin sheath in the PLA/AA/Li and PLA/AA/Li/cell groups compared with the control (CTR) group. In the CTR group, the injured area was almost completely filled by fibrous connective tissues. In the PLA/AA/Li and PLA/AA/Li/cell groups, a large number of myelinated axons (yellow arrows), low vacuolation (black arrows), and fibrosis were observed in the trauma area. Yellow dotted line area: nerve fibers. **b** Immunohistochemical staining of sciatic nerves 6-week postsurgery with anti-NF200, anti-S100B, and anti-SOX10 antibodies. Increased expression of NF200, S100B, and SOX10 was seen in the PLA/AA/Li and PLA/AA/Li/cell groups compared with the CTR group. Scale bars represent 50 μm. **c** Toluidine blue staining of sciatic nerves 6-week postsurgery. The PLA/AA/Li and PLA/AA/Li/cell groups had more arranged, distinct, and bundled myelinated axons than the CTR group. Yellow arrows: typical axons (axons with evident blue annulae); green arrows: degenerating axons (less distinct axons and myelin debris); red arrows: regenerating axons (distinct and small diameter axons). Scale bars represent 50 μm. **d** Analysis of the number and diameter of myelinated axons 6-week postsurgery. As shown, the PLA/AA/Li and PLA/AA/Li/cell groups showed increased axon density, axon diameter, and G-ratio compared with the CTR group. The corresponding average diameters of the axons and fibers were evaluated using ImageJ software. All data are expressed as mean ± standard deviation (SD), n=10. $^{*}p < 0.05$, $^{**}p < 0.01$, $^{****}p < 0.0001$, one-way analysis of variance (ANOVA) with Tukey–Kramer test. ns: not significant. **e** Transmission electron micrographs of transverse sections of sciatic nerves taken 6 weeks after surgery. The sciatic nerve ultrastructure indicated that the myelinated nerve fibers of the PLA/AA/Li and PLA/AA/Li/cell groups were more regular and uniform in diameter and shape compared with those of the CTR group. Multiple unmyelinated axons (green arrows) surrounded by Remak Schwann cells (yellow arrows) grouped in Remak bundles. Myelin debris (thick black arrows) and vacuoles within the myelin structures (thin black arrows) were only observed in the CTR group. M: myelinated axons with regular myelin lamellae; white asterisk: Remak Schwann cell nucleus; yellow asterisks: myelinating Schwann cell nucleus. H&E: hematoxylin and eosin. PLA: polylactide; AA: acrylic acid; Li: lithium

by a thick layer of fibrotic tissue, and some chronic inflammatory cells, such as multinucleated giant cells, were evident (Fig. S4 in Supplementary Information). As expected, in the PLA/AA/Li and PLA/AA/Li/cell groups, the nerve injury area was decreased, nerve fibers were arranged more normally, and no obvious inflammatory cells were observed. Similar to the PLA/plasma and PLA/AA groups, a fibrotic layer surrounded the newly regenerated nerve tissues in these groups (Fig. 8a; Fig. S4 in Supplementary Information).

Our immunohistochemistry results showed a significantly increased expression of NF200 (a marker of myelinated nerve fibers), SOX10 and S100B (Schwann cell markers) in the regenerated nerve fibers of the PLA/AA/Li and PLA/AA/Li/cell groups compared with the CTR group, indicating a significant increase in myelinated nerve fibers 6-week postsurgery (Fig. 8b).

To further investigate the histological characteristics of the regenerating axons, the regenerating nerves were stained with toluidine blue, which stains the myelin sheath (Fig. 8c). We found an increased number of typical and regenerating axons (small diameter) within the nerves with normal characteristics, including more arranged, distinct, and bundled myelinated axons, in the Li-loaded ENS groups compared with the CTR group. Our quantification analysis demonstrated that the axon density and diameter were significantly increased in the PLA/AA/Li ($(13.23 \pm 0.45) \times 10^3/\text{mm}^2$ and (6.30 ± 0.53) μm, respectively) and PLA/AA/Li/cell groups ($(13.97 \pm 0.15) \times 10^3/\text{mm}^2$ and (6.52 ± 0.52) μm, respectively) compared with those in the CTR group ($(5.99 \pm 0.13) \times 10^3/\text{mm}^2$ and (3.62 ± 0.08) μm, respectively). In addition, the G-ratio (the degree of axonal myelination) in the PLA/AA/Li/cell group (0.60 ± 0.04, $p = 0.0433$) was significantly increased compared with that in the CTR group (0.42 ± 0.01) (Fig. 8d).

TEM analysis of regenerating nerves 6-week postsurgery confirmed the above results and showed that the regenerated nerves in the PLA/AA/Li and PLA/AA/Li/cell groups were more organized and uniform in diameter and shape compared with those in the CTR group (Fig. 8e). Moreover, we observed Remak Schwann cells in the nerve sections of the PLA/AA/Li and PLA/AA/Li/cell groups, indicating that the nerves of these groups were in the regenerating phase.

Together, these findings indicate that the improved axonal regeneration in the Li-loaded ENSs leads to structural arrangements that resemble the intact sciatic nerve. In addition, because Li-containing scaffolds with/without cells had almost the same regenerative effects, this suggests that Li is the main factor in our scaffold that contributes to sciatic nerve regeneration.

Discussion

Recently, tissue engineering using polymeric scaffolds with or without live cells has provided an alternative therapy to traditional transplantation methods. Although different structures and biomaterials have been proposed for PNI treatment, their poor outcomes have initiated further research. The aim of the present study was to design a novel scaffold with a desirable electrospun nanofiber topography and the ability to release Li to activate Wnt/β-catenin signaling toward Schwann cell differentiation and axonal regeneration in an animal model of PNI.

In this study, we fabricated Li-loaded ENSs using an ion-exchange technique in which the incorporation of negatively charged groups functionalized polymeric materials [30, 46, 47]. PLA was first functionalized by carboxyl groups to provide cation-exchange properties, after which the Li ions were exchanged with protons. Among our fabricated scaffolds, the 10% AA-grafted ENS showed the best characteristics, including its 11-d release capability. Unlike the localized delivery method [29], which can result in the rapid release of a significant amount of Li in a short time and thus has toxicity concerns, our gradual release method provides a range of Li concentrations that are not within the toxic range (Figs. 2d and 2f). Interestingly, we observed strong differentiation of hADMSCs into SCLCs when the cells were cultured on 3D ENSs containing Li compared with those cultured on ENSs without Li (Fig. 5).

Further investigation of the effectiveness of these scaffolds was performed in an animal model of PNI. In the present study, we developed an animal model of crush injury to mimic persistent nerve injuries such as entrapment neuropathy and nerve crush injury, which account for 80% of PNIs [1]. To evaluate the nerve regeneration and recovery, behavioral, electrophysiological, and histological analyses were performed after implantation of ENSs in the injured location.

Our behavioral analyses showed that the regeneration rate in the animals who received Li-loaded ENSs was significantly increased compared with that of the control group and other studies using the same animal model [1, 48, 49]. Unlike the others [1, 6, 50, 51], we used short intervals for the behavioral tests; therefore, we were able to show more precisely the improved sensory, motor, and sensory-motor function, starting from the 2nd week after the nerve injury. To the best of our knowledge, our study is the first to show this rapid improvement in behavioral functions, which was possibly due to the high concentration of Li released during the first 2 weeks after implantation.

Our electrophysiological analyses of the gastrocnemius muscle demonstrated that the CMAP and NCV values were significantly higher in the Li-loaded ENSs group than in the CTR group. Generally, these factors collectively influence the speed at which electrical signals are conducted along the nerve fibers. The CMAP is believed to be influenced by the diameter of the nerve as it directly affects the number of neurons contributing to the response. The NCV, on the other hand, is correlated with several factors, including nerve fiber diameter, myelin thickness (which affects the speed of signal transmission), and the distance between the nodes of Ranvier (known as the internode distance). In another electrophysiological characteristic, the TL value, which signifies the time from stimulation to the response onset, was decreased in the Li-loaded ENSs groups compared with that of the CTR group. This result was indicative of the decreased conduction time from the stimulation point to the distal end, as well as the transmission time across the neuromuscular junction. Therefore, consistent with the results of the behavioral analysis, these results indicated that Li-loaded ENSs (with or without cells) promoted axonal regeneration and muscle reinnervation by increasing the myelin thickness, conduction speed, and the number of neurons.

Our histological analyses revealed a lower grade of fibrosis, higher axon density, and prominent increase in myelinated nerve fibers and Schwann cells in the nerve sections of animals implanted with Li-loaded ENSs compared with those of the control group and other studies [50]. Moreover, evaluation of the weight ratio of the gastrocnemius muscles from the affected and unaffected sides showed almost no muscle atrophy in the Li-loaded ENS groups, although it has been reported by others [29, 50]. The TEM micrograph showed that there were some cells with characteristics of nonmyelinating Remak Schwann cells, which have been previously reported to undergo a transformation to a specialized cell type. Therefore, they generated necessary signals and spatial cues that actively facilitated the repair process of the nerve [52]. The presence of Remak Schwann cells distal to the nerve damage further suggests that the nerves of the Li-loaded ENS groups were in the regenerating phase. Therefore, in line with the results of the behavioral and electrophysiological tests, our histological results showed that implantation of Li-loaded ENSs to the site of injury could enhance nerve regeneration and remyelination. Because rapid nerve regeneration was demonstrated in our behavioral tests, further histological analysis at more time points, especially as early as 2 weeks after surgery, could produce more useful data for a better clarification of the details of the repair mechanism.

Our results from both in vitro and in vivo experiments showed that the expression levels of the Schwann-specific markers S100B (a marker of most Schwann cell stages), GFAP and SOX10 (early markers), and GAP43 (an end-stage marker) (Figs. 5 and 8b) were increased by Li-containing scaffolds, indicating that Li promoted Schwann cell differentiation. This result is consistent with those of other studies that showed that Li not only stimulated the expression of myelin genes but also induced the differentiation of SCs [24, 25]. Considering the central role of Schwann cells in peripheral nerve regeneration, we could claim that Li released from our implanted scaffold affected Schwann cell differentiation of both local and transplanted cells in the injured nerve.

From the in vivo results presented in this study, it can be inferred that Li is the main element of our fabricated scaffold that contributes to sciatic nerve regeneration. Li, an antidepressant agent, inhibits GSK3β and activates the Wnt/β-catenin signaling pathway. Several studies have shown that the Wnt/β-catenin signaling pathway is a key element in myelin gene expression and myelinogenesis [10, 53–55], a positive regulator of the remyelination process [56, 57], and an enhancer of the viability, proliferation, and differentiation of Schwann cells [26, 58]. In our experiment, the 10% AA-grafted ENS had an 11-d Li release capacity ranging from 0.02 to (3.64 ± 0.10) mmol/L, which was in the range of concentration that upregulated the expression of *c-Myc* and *cyclinD1* (Wnt/β-catenin target genes) (Fig. 2g). It should be noted that despite the initial peak release of Li on the 1st day, Li release, even at its minimum concentration (0.02 mmol/L), within the last days of release remained sufficiently potent to activate the Wnt/β-catenin signaling pathway (Fig. 2g). Furthermore, due to the less aqueous environment in vivo, the release rate would be even lower [6], which would prolong the Li release window, a feature that can provide even better conditions for regeneration. Therefore, although further and more detailed studies are needed, our results suggest that Li exerts its effect by activating the Wnt/β-catenin signaling pathway.

Our behavioral, electrophysiological, and histological results showed that the cell-free Li-containing scaffolds caused regeneration of the injured sciatic nerve to almost the same extent as the cell-seeded scaffolds. While several studies have demonstrated the advantages of using cell-seeded scaffolds over cell-free ones [59], others have highlighted the drawbacks of cell transplantation and have suggested promising alternatives [60]. The discrepancy between these findings could be attributed to the number of transplanted cells, cell damage caused by the transplantation, and interactions between the transplanted cells and the host environment. Therefore, further research is required to address this question.

Conclusions

In this study, an electrospun scaffold grafted with polyacrylic acid was designed as a new scaffold with the ability to release stable and adjustable Li ions through an ion-exchange mechanism. Providing both biophysical and biochemical signals simultaneously, our fabricated scaffold not only provides an appropriate condition to induce and promote Schwann cell differentiation of hADMSCs but also accelerates the axonal regeneration and functional recovery of peripheral nerves with a low grade of fibrosis and myoatrophy. A closer look at our results clearly shows the pivotal impact of Li versus the scaffold alone in nerve regeneration. Acting probably through activation of the Wnt/β-catenin signaling pathway, Li may recruit local immune cells and/or stem/progenitor/Schwann cells to the injury site and employ them for peripheral nerve regeneration. Therefore, our fabricated ENS can be offered as a promising scaffold for both cell replacement and cell-free therapies in nerve tissue engineering applications and provides a new insight into Schwann cell-related diseases.

Supplementary Information The online version contains supplementary material available at https://doi.org/10.1007/s42242-024-00304-3.

Acknowledgements We wish to thank the funding support from the University of Tehran and the Iran National Science Foundation (INSF No. 97,012,418). The graphic abstract was created by Biorender.

Author contributions BD contributed to conceptualization, methodology, investigation, formal analysis, data curation, validation, writing-original draft, and writing-review and editing; BZ was involved in conceptualization, data curation, visualization, funding acquisition, resources, writing-review and editing, and supervision; IS performed conceptualization, resources, and supervision; APT was responsible for conceptualization, resources, and writing-review and editing; RKS contributed to investigation and data curation.

Data availability The data supporting the findings of this study are available from the corresponding authors upon reasonable request.

Declarations

Conflict of interest The authors declare that they have no conflict of interest.

Ethical approval All experiments were approved by the Research Committee of the College of Science, University of Tehran (approval No. 6104040.6.054). All procedures were performed according to Ethics Committee guidelines and regulations of the College of Science, University of Tehran. For isolation of primary human MSCs, informed consent was obtained from all subjects or their legal guardians. All in vivo methods are reported in accordance with the ARRIVE (Animal Research: Reporting of In Vivo Experiments) guidelines.

References

1. Suzuki K, Tanaka H, Ebara M et al (2017) Electrospun nanofiber sheets incorporating methylcobalamin promote nerve regeneration and functional recovery in a rat sciatic nerve crush injury model. Acta Biomater 53:250–259. https://doi.org/10.1016/j.actbio.2017.02.004
2. Hussain G, Wang J, Rasul A et al (2020) Current status of therapeutic approaches against peripheral nerve injuries: a detailed story from injury to recovery. Int J Biol Sci 16(1):116–134. https://doi.org/10.7150/ijbs.35653
3. Soto PA, Vence M, Piñero GM et al (2021) Sciatic nerve regeneration after traumatic injury using magnetic targeted adipose-derived mesenchymal stem cells. Acta Biomater 130:234–247. https://doi.org/10.1016/j.actbio.2021.05.050
4. Nocera G, Jacob C (2020) Mechanisms of Schwann cell plasticity involved in peripheral nerve repair after injury. Cell Mol Life Sci 77(20):3977–3989. https://doi.org/10.1007/s00018-020-03516-9
5. Chrząszcz P, Derbisz K, Suszyński K et al (2018) Application of peripheral nerve conduits in clinical practice: a literature review. Neurol Neurochir Pol 52(4):427–435. https://doi.org/10.1016/j.pjnns.2018.06.003
6. Bu YZ, Wang XH, Li LX et al (2020) Lithium loaded octa-poly(ethylene glycol) based adhesive facilitates axon regeneration and reconnection of transected peripheral nerves. Adv Healthc Mater 9(13):e2000268. https://doi.org/10.1002/adhm.202000268
7. Regas I, Loisel F, Haight H et al (2020) Functionalized nerve conduits for peripheral nerve regeneration: a literature review. Hand Surg Rehabil 39(5):343–351. https://doi.org/10.1016/j.hansur.2020.05.007
8. Ma Y, Gao HC, Wang H et al (2021) Engineering topography: effects on nerve cell behaviors and applications in peripheral nerve repair. J Mater Chem B 9(32):6310–6325. https://doi.org/10.1039/d1tb00782c
9. Liao DP, Li XJ, Dong Y et al (2017) The role of Wnt/β-catenin signaling pathway in the transdifferentiation from periodontal ligament stem cells to Schwann cells. Cell Reprogram 19(6):384–388. https://doi.org/10.1089/cell.2017.0017
10. Tawk M, Makoukji J, Belle M et al (2011) Wnt/β-catenin signaling is an essential and direct driver of myelin gene expression and myelinogenesis. J Neurosci 31(10):3729–3742. https://doi.org/10.1523/JNEUROSCI.4270-10.2011
11. Grigoryan T, Stein S, Qi JJ et al (2013) Wnt/Rspondin/β-catenin signals control axonal sorting and lineage progression in Schwann cell development. Proc Natl Acad Sci USA 110(45):18174–18179. https://doi.org/10.1073/pnas.1310490110
12. Phiel CJ, Klein PS (2001) Molecular targets of lithium action. Annu Rev Pharmacol Toxicol 41(1):789–813. https://doi.org/10.1146/annurev.pharmtox.41.1.789
13. Kuffler DP (2022) Can lithium enhance the extent of axon regeneration and neurological recovery following peripheral nerve trauma? Neural Regener Res 17(5):948–952. https://doi.org/10.4103/1673-5374.324830
14. Basselin M, Villacreses NE, Lee HJ et al (2007) Chronic lithium administration attenuates up-regulated brain arachidonic acid metabolism in a rat model of neuroinflammation. J Neurochem 102(3):761–772. https://doi.org/10.1111/j.1471-4159.2007.04593.x
15. Chuang DM (2005) The antiapoptotic actions of mood stabilizers: molecular mechanisms and therapeutic potentials. Ann NY Acad Sci 1053(1):195–204. https://doi.org/10.1196/annals.1344.018
16. Chiu CT, Chuang DM (2011) Neuroprotective action of lithium in disorders of the central nervous system. J Cent South Univ (Med Sci) 36(6):461–475. https://doi.org/10.3969/j.issn.1672-7347.2011.06.001
17. Yasuda S, Liang MH, Marinova Z et al (2009) The mood stabilizers lithium and valproate selectively activate the promoter IV of brain-derived neurotrophic factor in neurons. Mol Psychiatr 14(1):51–59. https://doi.org/10.1038/sj.mp.4002099
18. Fu R, Tang Y, Ling ZM et al (2014) Lithium enhances survival and regrowth of spinal motoneurons after ventral root avulsion. BMC Neurosci 15(1):84. https://doi.org/10.1186/1471-2202-15-84
19. Noble W, Planel E, Zehr C et al (2005) Inhibition of glycogen synthase kinase-3 by lithium correlates with reduced tauopathy and degeneration in vivo. Proc Natl Acad Sci USA 102(19):6990–6995. https://doi.org/10.1073/pnas.0500466102
20. Arraf Z, Youdim MBH (2004) Prevention of MPTP (*N*-methyl-4-phenyl-1,2,3,6-tetrahydropyridine) dopaminergic neurotoxicity in mice by chronic lithium: involvements of Bcl-2 and Bax.

Neuropharmacology 46(8):1130–1140. https://doi.org/10.1016/j.neuropharm.2004.02.005

21. Wei H, Qin ZH, Senatorov VV et al (2001) Lithium suppresses excitotoxicity-induced striatal lesions in a rat model of Huntington's disease. Neuroscience 106(3):603–612. https://doi.org/10.1016/s0306-4522(01)00311-6
22. van Eijk RPA, Jones AR, Sproviero W et al (2017) Meta-analysis of pharmacogenetic interactions in amyotrophic lateral sclerosis clinical trials. Neurology 89(18):1915–1922. https://doi.org/10.1212/WNL.0000000000004606
23. de Sarno P, Axtell RC, Raman C et al (2008) Lithium prevents and ameliorates experimental autoimmune encephalomyelitis. J Immunol 181(1):338–345. https://doi.org/10.4049/jimmunol.181.1.338
24. Makoukji J, Belle M, Meffre D et al (2012) Lithium enhances remyelination of peripheral nerves. Proc Natl Acad Sci USA 109(10):3973–3978. https://doi.org/10.1073/pnas.1121367109
25. Chen YX, Weng J, Han DY et al (2016) GSK3β inhibition accelerates axon debris clearance and new axon remyelination. Am J Transl Res 8(12):5410–5420
26. Gu XK, Li XR, Lu ML et al (2020) Lithium promotes proliferation and suppresses migration of Schwann cells. Neural Regener Res 15(10):1955–1961. https://doi.org/10.4103/1673-5374.280324
27. Zhang LQ, Zhang WM, Deng LX et al (2018) Transplantation of a peripheral nerve with neural stem cells plus lithium chloride injection promote the recovery of rat spinal cord injury. Cell Transplant 27(3):471–484. https://doi.org/10.1177/0963689717752945
28. Ala M, Mohammad Jafari R, Nematian H et al (2021) Neuroprotective effect of intravitreal single-dose lithium chloride after optic nerve injury in rats. Curr Eye Res 46(4):558–567. https://doi.org/10.1080/02713683.2020.1808999
29. Lin YC, Oh SJ, Marra KG (2013) Synergistic lithium chloride and glial cell line-derived neurotrophic factor delivery for peripheral nerve repair in a rodent sciatic nerve injury model. Plast Reconstr Surg 132(2):251e–262e. https://doi.org/10.1097/PRS.0b013e31829588cf
30. Shabani I, Haddadi-Asl V, Soleimani M et al (2014) Ion-exchange polymer nanofibers for enhanced osteogenic differentiation of stem cells and ectopic bone formation. ACS Appl Mater Interfaces 6(1):72–82. https://doi.org/10.1021/am404500c
31. Razavi S, Mardani M, Kazemi M et al (2013) Effect of leukemia inhibitory factor on the myelinogenic ability of Schwann-like cells induced from human adipose-derived stem cells. Cell Mol Neurobiol 33(2):283–289. https://doi.org/10.1007/s10571-012-9895-2
32. Dolatyar B, Zeynali B, Shabani I et al (2023) High-efficient serum-free differentiation of trabecular meshwork mesenchymal stem cells into Schwann-like cells on polylactide electrospun nanofibrous scaffolds. Neurosci Lett 813:137417. https://doi.org/10.1016/j.neulet.2023.137417
33. Hedayati S, Parvaneh Tafreshi A, Moradi N et al (2018) Inhibition of transforming growth factor-β signaling pathway enhances the osteogenic differentiation of unrestricted somatic stem cells. J Cell Biochem 119(11):9327–9333. https://doi.org/10.1002/jcb.27209
34. Munir H, Ward LS, Sheriff L et al (2017) Adipogenic differentiation of mesenchymal stem cells alters their immunomodulatory properties in a tissue-specific manner. Stem Cells 35(6):1636–1646. https://doi.org/10.1002/stem.2622
35. Dzobo K, Turnley T, Wishart A et al (2016) Fibroblast-derived extracellular matrix induces chondrogenic differentiation in human adipose-derived mesenchymal stromal/stem cells in vitro. Int J Mol Sci 17(8):1259. https://doi.org/10.3390/ijms17081259
36. Sahebdel F, Parvaneh Tafreshi A, Arefian E et al (2022) Wnt/β-catenin signaling pathway is involved in early dopaminergic differentiation of trabecular meshwork-derived mesenchymal stem cells. J Cell Biochem 123(6):1120–1129. https://doi.org/10.1002/jcb.30269
37. Mohammadi Amirabad L, Massumi M, Shamsara M et al (2017) Enhanced cardiac differentiation of human cardiovascular disease patient specific induced pluripotent stem cells by applying unidirectional electrical pulses using aligned electroactive nanofibrous scaffolds. ACS Appl Mater Interfaces 9(8):6849–6864. https://doi.org/10.1021/acsami.6b15271
38. Kehtari M, Beiki B, Zeynali B et al (2019) Decellularized Wharton's jelly extracellular matrix as a promising scaffold for promoting hepatic differentiation of human induced pluripotent stem cells. J Cell Biochem 120(4):6683–6697. https://doi.org/10.1002/jcb.27965
39. Navarro X (2016) Functional evaluation of peripheral nerve regeneration and target reinnervation in animal models: a critical overview. Eur J Neurosci 43(3):271–286. https://doi.org/10.1111/ejn.13033
40. Nishimoto S, Tanaka H, Okamoto M et al (2015) Methylcobalamin promotes the differentiation of Schwann cells and remyelination in lysophosphatidylcholine-induced demyelination of the rat sciatic nerve. Front Cell Neurosci 9:298. https://doi.org/10.3389/fncel.2015.00298
41. Bain JR, Mackinnon SE, Hunter DA (1989) Functional evaluation of complete sciatic, peroneal, and posterior tibial nerve lesions in the rat. Plast Reconstr Surg 83(1):129–136. https://doi.org/10.1097/00006534-198901000-00024
42. Sorrenti V, Cecchetto C, Maschietto M et al (2021) Understanding the effects of anesthesia on cortical electrophysiological recordings: a scoping review. Int J Mol Sci 22(3):1286. https://doi.org/10.3390/ijms22031286
43. Mirakhori F, Zeynali B, Tafreshi AP et al (2013) Lithium induces follicular atresia in rat ovary through a GSK-3β/β-catenin dependent mechanism. Mol Reprod Dev 80(4):286–296. https://doi.org/10.1002/mrd.22163
44. Imani F, Karimi-Soflou R, Shabani I et al (2021) PLA electrospun nanofibers modified with polypyrrole-grafted gelatin as bioactive electroconductive scaffold. Polymer 218:123487. https://doi.org/10.1016/j.polymer.2021.123487
45. Dautoo UK, Shandil Y, Ranote S et al (2022) New efficient poly(acrylic acid)-based bifunctional Cu^{2+} ions adsorbents. Colloids Surf A 635:128090. https://doi.org/10.1016/j.colsurfa.2021.128090
46. Kawai T, Ohtsuki C, Kamitakahara M et al (2004) Coating of an apatite layer on polyamide films containing sulfonic groups by a biomimetic process. Biomaterials 25(19):4529–4534. https://doi.org/10.1016/j.biomaterials.2003.11.039
47. Miyazaki T, Ohtsuki C, Akioka Y et al (2003) Apatite deposition on polyamide films containing carboxyl group in a biomimetic solution. J Mater Sci Mater Med 14(7):569–574. https://doi.org/10.1023/a:1024000821368
48. Sun WJ, Sun CK, Lin H et al (2009) The effect of collagen-binding NGF-β on the promotion of sciatic nerve regeneration in a rat sciatic nerve crush injury model. Biomaterials 30(27):4649–4656. https://doi.org/10.1016/j.biomaterials.2009.05.037
49. Renno WM, Al-Maghrebi M, Alshammari A et al (2013) (−)-Epigallocatechin-3-gallate (EGCG) attenuates peripheral nerve degeneration in rat sciatic nerve crush injury. Neurochem Int 62(3):221–231. https://doi.org/10.1016/j.neuint.2012.12.018
50. Kocman AE, Dag I, Sengel T et al (2020) The effect of lithium and lithium-loaded hyaluronic acid hydrogel applications on nerve regeneration and recovery of motor functions in peripheral nerve injury. Rend Fis Acc Lincei 31(3):889–904. https://doi.org/10.1007/s12210-020-00919-5
51. Jahromi HK, Farzin A, Hasanzadeh E et al (2020) Enhanced sciatic nerve regeneration by poly-L-lactic acid/multi-wall carbon nanotube neural guidance conduit containing Schwann cells and curcumin encapsulated chitosan nanoparticles in rat. Mater Sci Eng

C Mater Biol Appl 109:110564. https://doi.org/10.1016/j.msec.2019.110564
52. Jessen KR, Mirsky R (2016) The repair Schwann cell and its function in regenerating nerves. J Physiol 594(13):3521–3531. https://doi.org/10.1113/JP270874
53. Chew LJ, Shen WP, Ming XT et al (2011) SRY-box containing gene 17 regulates the Wnt/β-catenin signaling pathway in oligodendrocyte progenitor cells. J Neurosci 31(39):13921–13935. https://doi.org/10.1523/JNEUROSCI.3343-11.2011
54. Meffre D, Massaad C, Grenier J (2015) Lithium chloride stimulates PLP and MBP expression in oligodendrocytes via Wnt/β-catenin and Akt/CREB pathways. Neuroscience 284:962–971. https://doi.org/10.1016/j.neuroscience.2014.10.064
55. Hichor M, Sampathkumar NK, Montanaro J et al (2017) Paraquat induces peripheral myelin disruption and locomotor defects: crosstalk with LXR and Wnt pathways. Antioxidant Redox Signal 27(3):168–183. https://doi.org/10.1089/ars.2016.6711
56. Makoukji J, Meffre D, Grenier J et al (2011) Interplay between LXR and Wnt/β-catenin signaling in the negative regulation of peripheral myelin genes by oxysterols. J Neurosci 31(26):9620–9629. https://doi.org/10.1523/JNEUROSCI.0761-11.2011
57. Fancy SPJ, Baranzini SE, Zhao C et al (2009) Dysregulation of the Wnt pathway inhibits timely myelination and remyelination in the mammalian CNS. Genes Dev 23(13):1571–1585. https://doi.org/10.1101/gad.1806309
58. Yang L, Yang F, Liu JR et al (2018) Protective effect of lithium on Schwann cell transplantation via Wnt/beta-catenin signaling pathway after spinal cord injury in vitro and vivo. Int J Clin Exp Med 11(10):10487–10495
59. Sun X, Zhu Y, Yin HY et al (2018) Differentiation of adipose-derived stem cells into Schwann cell-like cells through intermittent induction: potential advantage of cellular transient memory function. Stem Cell Res Ther 9(1):133. https://doi.org/10.1186/s13287-018-0884-3
60. Rao ZL, Lin ZD, Song PP et al (2022) Biomaterial-based Schwann cell transplantation and Schwann cell-derived biomaterials for nerve regeneration. Front Cell Neurosci 16:926222. https://doi.org/10.3389/fncel.2022.926222

Authors and Affiliations

Banafsheh Dolatyar[1] · Bahman Zeynali[1] · Iman Shabani[2] · Azita Parvaneh Tafreshi[1,3] · Reza Karimi-Soflou[2]

✉ Bahman Zeynali
zeynalib@ut.ac.ir

✉ Iman Shabani
shabani@aut.ac.ir

[1] Developmental Biology Laboratory, School of Biology, College of Science, University of Tehran, Tehran 1417614411, Iran

[2] Department of Biomedical Engineering, Amirkabir University of Technology (Tehran Polytechnic), Tehran 1591634311, Iran

[3] Department of Molecular Medicine, Faculty of Medical Biotechnology, National Institute of Genetic Engineering and Biotechnology, Tehran 1497716316, Iran